Journal of Nanobiotechnology

RESEARCH Open Access

Nanoparticle-mediated SIRT1 inhibition suppresses M2 macrophage polarization and hepatocarcinogenesis in chronic hepatitis B

He Zhang[1,2†], Feng Yuan[3†], Nan Zhao[4†], Wenqiang Tang[5†], Pengwei Zhao[6], Chunfa Liu[1], Shan Chen[1], Xiaolin Hou[1*], Changyou Xia[2*] and Jun Chu[1,5*]

Abstract

Hepatocellular carcinoma (HCC) is a major complication of chronic hepatitis B (CHB), with macrophage M2 polarization playing a critical role in shaping the tumor-promoting hepatic immune microenvironment. Sirtuin 1 (SIRT1) has been implicated in immune modulation and liver carcinogenesis. This study investigates the potential of Mimetic Nanoparticles (MNPs) for delivering SIRT1 inhibitors to regulate macrophage polarization and remodel the hepatic immune microenvironment, aiming to prevent HCC development post-CHB. A transgenic mouse model of CHB was established, and RNA sequencing (RNA-seq) and proteomics analyses revealed significant dysregulation of genes associated with M2 macrophage polarization, particularly SIRT1. Functional enrichment analysis highlighted key pathways, including PI3K-Akt and NF-κB, that contribute to CHB-driven immune alterations. Synthesized and characterized MNPs successfully delivered SIRT1 inhibitors, effectively inhibiting M2 macrophage polarization in vitro. In vivo administration of MNPs-SIRT1-FN significantly reduced M2 macrophage infiltration and suppressed tumor growth. These findings suggest that nanoparticle-mediated SIRT1 inhibition is a promising strategy for immunomodulation and HCC prevention in CHB patients. This study provides novel insights into nanoparticle-based immunotherapy for CHB-related HCC and highlights a potential therapeutic avenue for liver cancer prevention.

Introduction

Hepatocellular carcinoma (HCC) is one of the leading causes of cancer-related deaths worldwide, with high incidence and mortality rates [1–3]. This is particularly evident in developing countries, where the prevalence of chronic hepatitis B (CHB) significantly increases HCC incidence [4, 5]. Although antiviral treatments have made considerable progress in controlling hepatitis B virus (HBV) infections and reducing the incidence of acute hepatitis, CHB patients remain at high risk for cirrhosis and HCC [6–8]. Notably, the chronic inflammatory response and persistent viral replication in CHB are key

†He Zhang, Feng Yuan, Nan Zhao and Wenqiang Tang contributed equally to this work.

*Correspondence:
Xiaolin Hou
20097303@bua.edu.cn
Changyou Xia
xiachangyou@caas.cn
Jun Chu
tongtongchujun@163.com

Full list of author information is available at the end of the article

Graphical Abstract

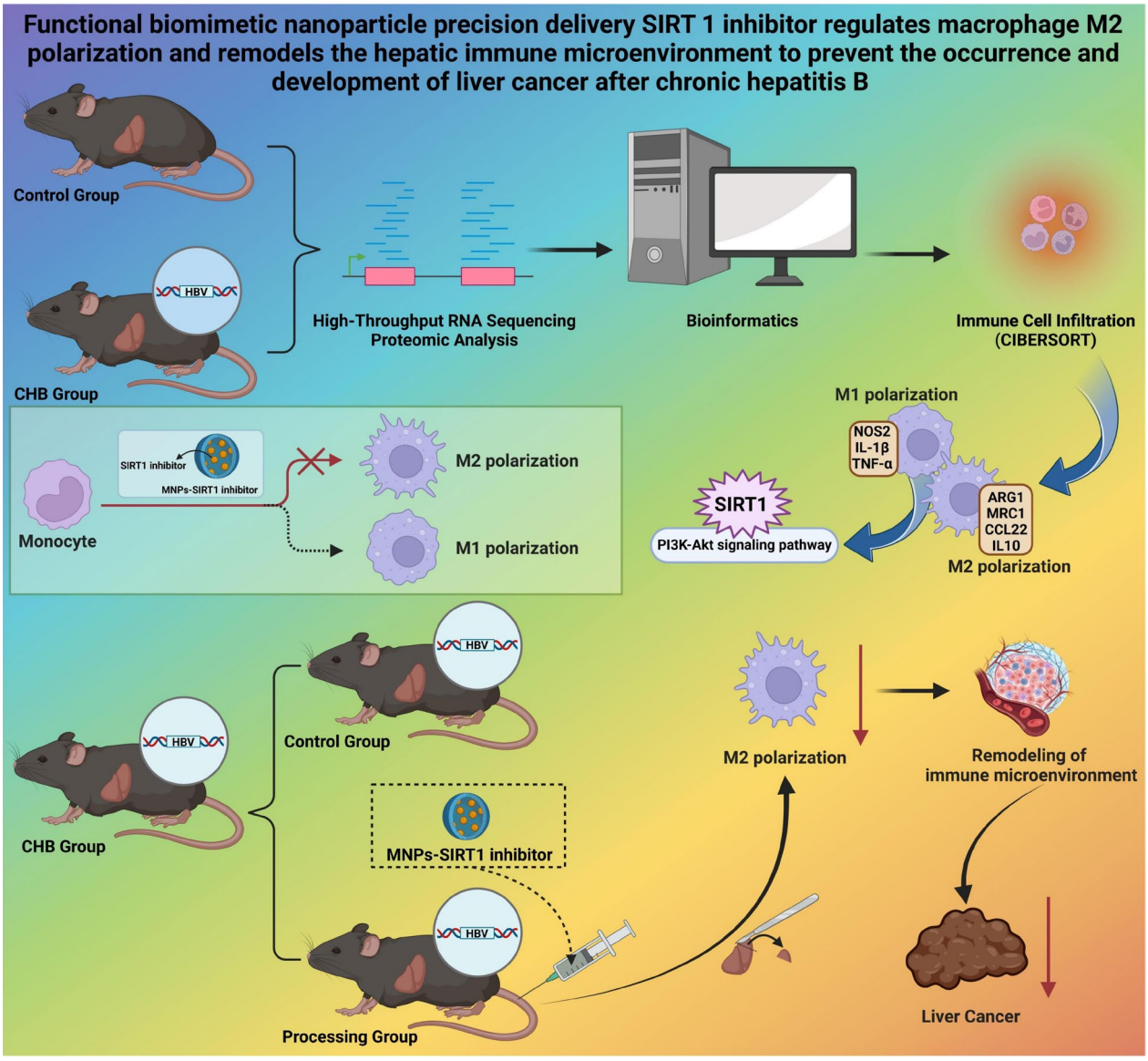

Keywords Nanoparticles, SIRT1 Inhibition, Macrophage polarization, Chronic hepatitis B, Hepatocellular carcinoma

factors driving the progression to HCC [9–11]. Therefore, exploring new therapeutic strategies to prevent CHB from progressing to HCC is of significant clinical importance, as it can improve patient survival rates and reduce the healthcare burden associated with HCC [12, 13].

Currently, the primary treatment options for HCC include surgical resection, radiation therapy, chemotherapy, and targeted therapy [14, 15]. However, these conventional treatments often come with significant side effects, and their efficacy varies among individuals [16–18]. In particular, for advanced-stage HCC, high tumor recurrence rates and drug resistance severely limit treatment effectiveness [19–21]. Although surgical resection is the preferred treatment for early-stage HCC, many patients are diagnosed at intermediate or advanced stages, missing the optimal window for surgery [22–24]. Radiation and chemotherapy can damage normal liver tissue, increasing patient discomfort [14, 25, 26]. While targeted therapy has improved treatment outcomes to some extent, issues with target specificity and patient tolerance remain significant challenges. Consequently, the search for new methods to effectively regulate the hepatic

immune microenvironment has become a focal point in HCC treatment research.

In recent years, the advent of immunotherapy has brought new hope for HCC patients. In particular, the combination of immune checkpoint inhibitors (ICIs) with macromolecular anti-angiogenesis drugs has made milestone progress [27]. The global multicenter phase III clinical trial IMBrave-150 has shown that compared to sorafenib, the combination of atezolizumab and bevacizumab significantly improves the median overall survival (MoS) of advanced hepatocellular carcinoma (HCC) patients. Specifically, the MoS for the "T + A" regimen was 19.2 months, while sorafenib was 13.4 months, showing a statistically significant difference ($P < 0.001$) [28, 29]. In the perioperative period, immunotherapy has also demonstrated its unique advantages. The IMbrave050 study, as the first global trial exploring the use of anti-angiogenesis combined with immunotherapy for adjuvant treatment in HCC, provides the most compelling evidence available [30].

Macrophages play a crucial role in the hepatic immune microenvironment and can be categorized into M1 and M2 types based on their functional states [31, 32]. M1 macrophages exhibit pro-inflammatory properties by secreting large amounts of inflammatory cytokines such as TNF-α and IL-1β, which are involved in pathogen clearance and tissue repair [33–35]. Conversely, M2 macrophages possess anti-inflammatory and tissue repair functions, primarily by secreting anti-inflammatory cytokines such as IL-10 and TGF-β, thereby promoting tissue regeneration and repair [36–38]. In the context of CHB and HCC, excessive polarization of M2 macrophages is closely associated with HCC development. Their immunosuppressive role within the tumor microenvironment enables tumor cells to evade immune surveillance [39–41]. Therefore, regulating macrophage polarization, particularly inhibiting M2 polarization, may offer new strategies for the prevention and treatment of HCC.

In recent years, mimetic nanoparticles (MNPs) have shown immense potential in drug delivery [42, 43]. MNPs exhibit excellent biocompatibility and targeting capabilities, enabling efficient drug delivery to specific cells or tissues, thereby enhancing therapeutic efficacy and reducing side effects [44]. This study aims to use MNPs to deliver Sirtuin 1 (SIRT1) inhibitors, modulating macrophage M2 polarization to remodel the hepatic immune microenvironment, thereby preventing the progression of HCC following CHB. SIRT1, a deacetylase, plays a critical role in various biological processes (BP), including inflammation, metabolic regulation, and apoptosis. Inhibiting SIRT1 can effectively suppress macrophage M2 polarization, reduce immune suppression in the tumor microenvironment, and consequently inhibit tumor growth and metastasis.

The aim of this study is to investigate the mechanisms by which MNPs delivering SIRT1 inhibitors regulate macrophage M2 polarization and remodel the hepatic immune microenvironment. Using a CHB mouse model, we systematically evaluated the efficacy and molecular mechanisms of MNPs-SIRT1-FN in preventing the progression of HCC. Initially, high-throughput RNA Sequencing (RNA-seq) and proteomics analyses were conducted to identify Differentially Expressed Genes (DEGs) and proteins in CHB mice and their roles in hepatic pathology. Subsequently, bioinformatics tools were employed to screen and perform functional enrichment analysis of these DEGs and proteins, revealing key signaling pathways and BP. Finally, in vivo and in vitro experiments validated the inhibitory effects of MNPs-SIRT1-FN on macrophage M2 polarization and their preventive and therapeutic efficacy against HCC in the context of CHB. This study not only offers new strategies and approaches for the prevention and treatment of HCC but also highlights the potential of biomimetic nanotechnology in tumor immunotherapy, providing robust scientific evidence for clinical application. This research strategy could serve as a reference for treating other chronic inflammation-related cancers, possessing broad scientific and clinical significance.

Materials and methods

Ethics statement

All animal experiments conducted in this study strictly adhered to the "Guidelines for the Scientific Use of Animals" issued by the Ministry of Science and Technology. Prior to the experiments, approval was obtained from the Institutional Animal Care and Use Committee (approval number: BUA812403010). All procedures were designed to minimize animal suffering and to ensure that the number of animals used was the minimum required to achieve scientific validity.

Construction of a CHB-Induced HCC mouse model

Six- to eight-week-old transgenic C57BL/6 mice, specifically expressing the HBV gene, were obtained from Charles River Laboratories. The mice were housed under specific pathogen-free (SPF) conditions, with a 12-hour light/dark cycle and ad libitum access to food and water. Initially, liver damage was induced by intraperitoneal injection of diethylnitrosamine (DEN, 25 mg/kg). Subsequently, the HBV transgenic mice continued expressing the HBV gene to simulate the pathological state of chronic hepatitis B. To enhance the inflammatory response and promote model development, the immune microenvironment was modulated using immunoregulators (PD-1/PD-L1 antibodies). During this period, mice were regularly monitored for changes in body weight, liver function indicators (ALT, AST), and external

symptoms (reduced activity or changes in fur sheen). The mice were randomly divided into two groups: the treatment group (receiving injections of SIRT1 inhibitor-loaded MNPs) and the control group, with 10 mice in each group. The treatment group mice received tail vein injections of the MNPs, and their body weight and behavior were monitored for 24 h post-injection, and after 4 weeks of treatment, the mice were euthanized, and liver tissues were harvested for further experiments. The in vivo experimental procedure is detailed in Figure S1.

Liver function and histological analysis

Every two weeks, blood samples were collected from the tail vein, and levels of ALT and AST were measured using a Beckman Coulter automated biochemical analyzer. At the end of the experiment, all mice were euthanized with an overdose of carbon dioxide. Liver tissues were collected for Hematoxylin and Eosin (H&E) staining and immunohistochemical analysis. Immunohistochemistry was performed using antibodies against SIRT1 and CD206 (Abcam, UK), and images were captured and analyzed using a Nikon Eclipse Ti microscope (Nikon, Japan). Concurrently, antibodies targeting F4/80 were used in conjunction with antibodies against CD206 and CD80 (Abcam, UK) for immunofluorescence co-localization staining. The co-localization of the staining was observed using a confocal laser scanning microscope (CLSM, Leica TCS SP8).

RNA-seq

Total RNA was extracted from the liver tissues of both control and CHB groups using Trizol reagent (15596026, Invitrogen, USA). The integrity and purity of the extracted RNA were assessed with an Agilent 2100 Bioanalyzer (G2939B, Agilent, USA), ensuring an RNA integrity number (RIN) of no less than 7.0. High-throughput sequencing was performed on the Illumina HiSeq platform (Illumina, USA). The sequencing data underwent quality control and were aligned to the mouse reference genome using HISAT2 software. Gene expression levels were quantified with HTSeq-count. DEGs were identified using DESeq2 with criteria of $|\log FC| > 1$ and $p < 0.05$. The DEGs between the control and disease groups were visualized using volcano plots generated by the "ggplot2" package. All analyses were conducted in R version 4.3.1 (R Foundation for Statistical Computing).

Immune infiltration

Based on our expression profile, we used the R software packages "e1071" and "preprocessCore" in combination with the CIBERSORT algorithm to score 22 types of immune infiltrating cells. Statistical analysis and visualization were conducted using R version 4.2.1, with the "ggplot2" package employed for visualization.

Gene ontology (GO) and Kyoto encyclopedia of genes and genomes (KEGG) enrichment analysis

For gene set functional enrichment analysis, we utilized the R package org.Hs.eg.db (version 3.1.0) to obtain GO annotations for the genes, which served as the background for mapping the genes to the background set. The R package clusterProfiler (version 3.14.3) was used to perform the enrichment analysis and generate the gene set enrichment results. For KEGG pathway enrichment analysis, we retrieved the latest KEGG pathway gene annotations using the KEGG REST API, which also served as the background for mapping genes to the background set. The R package clusterProfiler (version 3.14.3) was again employed to conduct the enrichment analysis and obtain the results. The parameters were set with a minimum gene set size of 5, a maximum gene set size of 5000, a p-value of < 0.05, and an FDR of < 0.25. Data visualization was performed using the ggplot2 package.

Proteomics analysis

Total proteins were extracted from liver tissues of both the CHB and control groups using RIPA buffer (with protease inhibitors, Thermo Fisher Scientific, USA). Protein quantification was performed using the BCA Protein Assay Kit (23227, Thermo Fisher Scientific, USA). After enzymatic digestion, protein samples were analyzed using LC-MS/MS on a Q Exactive HF mass spectrometer (Thermo Fisher Scientific, USA). The proteomics data were processed with Proteome Discoverer software (Thermo Fisher Scientific, USA) to identify protein expression changes associated with HCC development and immune regulation.

Proteins with a $|\log FC| > 1$ and a p-value < 0.05 in the Student's t-test were considered significantly differentially expressed proteins (DEPs).

Materials and reagents

The materials and reagents used in this study include mesoporous silica (MCM-41) nanoparticles (Sigma-Aldrich, Product No. 691306); SIRT1 inhibitor EX-527 (Sigma-Aldrich, Product No. SML0546); 3-aminopropyltriethoxysilane (APTES) (Sigma-Aldrich, Product No. 440140); 1-ethyl-3-(3-dimethylaminopropyl) carbodiimide hydrochloride (EDC) (Sigma-Aldrich, Product No. E6383); N-hydroxysuccinimide (NHS) (Sigma-Aldrich, Product No. 130672); and fibronectin (FN) (Sigma-Aldrich, Product No. F2006). Other necessary chemical reagents and solvents, such as ethanol, dimethyl sulfoxide (DMSO), and phosphate-buffered saline (PBS), were also used.

Preparation of nanoparticles

Mesoporous silica was selected for this study due to its high surface area, excellent biocompatibility, tunable pore size, and ability to provide controlled drug release [45]. Additionally, its mature surface functionalization strategies allow for efficient loading and targeted delivery of SIRT1 inhibitors [46]. At room temperature, MCM-41 nanoparticles were dispersed in anhydrous ethanol, followed by the addition of APTES (5% v/v). The mixture was stirred for 12 h to achieve amination. The aminated nanoparticles were then collected by centrifugation (10,000 rpm, 10 min) and washed multiple times with anhydrous ethanol. Finally, the nanoparticles were vacuum-dried at 60 °C.

SIRT1 inhibitor loading

Aminated nanoparticles were dispersed in PBS, followed by the addition of EDC and NHS (molar ratio 1:1, final concentration 10 mM) and stirred for 30 min to activate the carboxyl groups. Given that EX527 shows high specificity for SIRT1 [47], and has been a commonly used inhibitor in SIRT1 research in recent years [48], we chose EX-527 as the SIRT1 inhibitor. The SIRT1 inhibitor EX-527 (final concentration 5 mM) was then added, and the reaction proceeded at room temperature for 12 h to form a covalent bond, loading the inhibitor onto the nanoparticle surface. The nanoparticles were collected by centrifugation and washed multiple times with PBS. The loaded nanoparticles were stored at 4 °C.

Fibronectin modification

Nanoparticles loaded with SIRT1 inhibitors were dispersed in PBS, followed by the addition of EDC and NHS (molar ratio 1:1, final concentration 10 mM). The mixture was stirred for 30 min to activate the carboxyl groups. Fibronectin (final concentration 2 mg/mL) was then added, and the reaction was allowed to proceed at room temperature for 12 h to covalently attach the fibronectin to the nanoparticle surface. The resulting fibronectin-modified MNPs (MNPs-SIRT1-FN) were obtained through multiple rounds of centrifugation and washing with PBS. The modified nanoparticles were stored at 4 °C.

Characterization

The morphology and size of the nanoparticles were observed using Transmission Electron Microscopy (TEM, JEOL JEM-2100 F). The particle size distribution and surface charge of the nanoparticles were measured using Dynamic Light Scattering (DLS, Malvern Zetasizer Nano ZS). The chemical modifications on the surface of the nanoparticles were analyzed by Fourier Transform Infrared Spectroscopy (FTIR, Thermo Nicolet iS50). The thermal stability of the nanoparticles was assessed using Thermogravimetric Analysis (TGA, TA Instruments Q500).

Encapsulation efficiency determination

The determination of encapsulation efficiency is conducted using high-performance liquid chromatography (HPLC, HPLC 1260, Agilent). Initially, a series of EX-527 standard solutions at different concentrations are prepared and analyzed via HPLC to establish a standard curve between concentration and peak area. Subsequently, the nanoparticles are treated with an appropriate solvent to release the encapsulated EX-527, and its concentration is determined using HPLC. Encapsulation efficiency (EE%) and drug loading (DL%) are calculated using formulas (1) and (2), respectively, by comparing the total amount of EX-527 added with the amount detected by HPLC, providing quantitative information about the drug encapsulation performance. Each value is measured three times.

Formula (1):

$$EE\ (\%\ w/w) = \frac{actual\ mass\ of\ drug\ in\ liposomes}{theoretical\ mass\ of\ drug\ in\ liposomes} \times 100\%$$

Formula (2):

$$\mathrm{DL}\ (\%\ \mathrm{w/w}) = \frac{\text{actual mass of drug in liposomes}}{\text{total mass of liposomes}} \times 100\%$$

Cell culture

Mouse macrophage cell line RAW 264.7 (ATCC TIB-71) was obtained for the study. The cells were cultured in DMEM medium supplemented with 10% fetal bovine serum (FBS, Gibco, USA) and 1% penicillin-streptomycin (Gibco, USA). Cultures were maintained at 37 °C in a humidified atmosphere of 5% CO_2. Normal human liver cells, L-O2 cells (iCell-h054, Cellverse Co., Ltd., Shanghai, China), are cultured in RPMI 1640 medium supplemented with 10% FBS and 1% penicillin-streptomycin at 37 °C under 5% CO_2 conditions.

In Vitro Cellular Uptake Experiment

L-O2 and RAW 264.7 cells were seeded into a 6-well plate at a density of 1×10^6 cells per well and incubated for 24 h. Fluorescently labeled MNPs-SIRT1-FN (FITC-labeled, Thermo Fisher Scientific, Product No.: F1303) were then added at a concentration of 50 μg/mL. The cells were further incubated for 2, 4, 8, and 24 h. Subsequently, the cells were collected and washed three times with PBS.

Prepared MNPs were added to the culture medium of RAW 264.7 macrophages, with different concentration groups set up: low concentration (10 μg/mL), medium concentration (50 μg/mL), and high concentration (100 μg/mL), along with a control group (untreated). After 24 h of incubation, subsequent analyses were performed.

In Vitro Biocompatibility Evaluation

Cell viability was determined using a live/dead cell staining kit (PF00007, Proteintech, USA). Specifically, L-O2 and RAW 264.7 cells were seeded at a density of 1.5×10^4 cells/cm² in 24-well plates and cultured with medium containing nanoparticles for 1, 3, and 7 days. After culturing, the cells were thoroughly washed with PBS and co-incubated with 200 μL of live/dead staining solution at room temperature for 30 min, followed by observation under a fluorescence microscope. To ensure the reproducibility of the results, experiments under each set of conditions were performed in triplicate.

Lysosomal escape capability assay

1×10^6 RAW 264.7 cells were seeded in 6-well plates and cultured overnight at 37 °C. Subsequently, nanoparticles labeled with Rhodamine B-PEG-NH_2 (abbreviated as RhB, R164232, Aladdin, Shanghai, China, https://www.aladdin-e.com/zh_cn/) were co-cultured with RAW 264.7 cells for 2 h and 6 hours. After co-culturing, the cells were washed and stained with Hoechst 33,342 (C0031, 1:100, Solarbio, Beijing, China) and Lyso-Tracker Green fluorescent probe (C1047S, Beyotime, Shanghai, China). All samples were observed by CLSM.

Observation with confocal laser scanning microscopy (CLSM)

RAW 264.7 cells that had taken up fluorescently labeled nanoparticles were fixed on coverslips using 4% paraformaldehyde for 15 min, followed by three washes with PBS. The coverslips were mounted with a mounting medium containing DAPI (Sigma-Aldrich, product number: D9542). The cellular uptake of nanoparticles was observed using a confocal laser scanning microscope (CLSM, Leica TCS SP8). Each experiment was repeated three times, and representative images were presented.

Cell polarization detection

Cells were collected and washed twice with PBS (Gibco, USA). The cells were then fixed with 4% paraformaldehyde (Sigma-Aldrich, USA) for 15 min. Specific antibodies (anti-CD206 and anti-Arg1, purchased from BioLegend) were used for staining. The stained cells were suspended in a flow cytometry buffer and analyzed using a flow cytometer (BD FACSAria™ III, BD Biosciences) to detect the expression of M2 macrophage markers, CD206 and Arg1.

The cell culture supernatant was collected, and the levels of cytokines IL-10 and TGF-β were measured using an Enzyme-Linked Immunosorbent Assay (ELISA) kit (R&D Systems) according to the manufacturer's instructions. Absorbance was read at 450 nm using a microplate reader (Bio-Rad, USA). The final measurements were reported as cytokine concentrations in picograms per milliliter (pg/mL).

RT-qPCR

RNA extraction and reverse transcription Under sterile conditions, total RNA was extracted from treated macrophages using Trizol reagent (Invitrogen, USA) according to the manufacturer's instructions. The purified RNA (at least 1 μg per experiment) served as the template for cDNA synthesis, which was performed using the PrimeScript RT reagent Kit (Takara Bio, Japan).

Real-Time Quantitative PCR RT-qPCR was conducted using the SYBR Green Master Mix (Thermo Fisher Scientific, USA) on the ABI 7500 Real-Time PCR system (Applied Biosystems, USA). The expression levels of the SIRT1 mRNA and M2 macrophage-related genes, such as Mrc1 and Arg1, were quantified, with GAPDH used as the reference gene. The PCR conditions were set as follows: initial denaturation at 95 °C for 5 min, followed by 40 cycles of 95 °C for 15 s and 60 °C for 30 s. Each sample was tested in at least triplicate to ensure the reliability of the data.

Western blot

Total protein was extracted from cells using RIPA buffer containing protease inhibitors (Beyotime, China). Protein concentration was determined with a BCA protein assay kit (Pierce, USA). Equal amounts of protein (at least 20 μg per sample) were separated by Sodium Dodecyl Sulfate Polyacrylamide Gel Electrophoresis (SDS-PAGE) and transferred to PVDF membranes (Millipore, USA). The membranes were blocked with 5% non-fat milk to prevent nonspecific binding and then incubated overnight at 4 °C with the following primary antibodies: anti-SIRT1, p-PI3K (ab191606, Abcam, UK), PI3K (ab154598, Abcam, UK), p-AKT (ab38449, Abcam, UK), AKT (ab8805, Abcam, UK), and the internal control β-actin (Abcam, UK). The next day, the membranes were incubated for 1 h with HRP-conjugated secondary antibodies (Jackson ImmunoResearch, USA). Signals were detected using a chemiluminescence detection system (Bio-Rad, USA), and images were captured and analyzed with ImageJ software (NIH, USA).

Immunofluorescence staining

The treated RAW 264.7 or mouse liver tissue was fixed with 4% paraformaldehyde (Sigma-Aldrich, USA) and permeabilized using 0.1% Triton X-100 (Sigma-Aldrich, USA). The cells were then incubated with the primary antibody against SIRT1 (Cell Signaling Technology, USA); CD206 (Cell Signaling Technology, USA); CD80 (Cell Signaling Technology, USA) or F4/80 (Cell Signaling Technology, USA), followed by incubation with the

secondary antibody Alexa Fluor 488 (Invitrogen, USA) or Alexa Fluor 549 (Invitrogen, USA). Observations were made using a confocal microscope (Leica TCS SP8, Germany), and image analysis was performed with LAS X software (Leica, Germany).

Analysis of immune microenvironment components

The distribution of immune cell subsets in the liver of both the treatment and control groups was analyzed using a flow cytometer (BD Biosciences, USA). Sample preparation involved treating liver tissue with collagenase and DNase, followed by staining with specific antibodies (e.g., F4/80, CD11b, CD86, CD206) for surface and intracellular markers. Flow cytometry data were analyzed using FlowJo software.

Statistical analysis methods

Statistical analyses in this study were performed using SPSS 25.0 and GraphPad Prism 8.0. All experimental data are presented as mean ± standard deviation (Mean ± SD). Group comparisons for cell and animal experiments were conducted using one-way analysis of variance (ANOVA), with statistical significance defined as $p < 0.05$. For multiple comparisons, Tukey's honestly significant difference (HSD) post hoc test was applied. If the assumptions of normality and homogeneity of variance were met, Student's t-test (for two groups) or one-way ANOVA (for three or more groups) was used. If these assumptions were not met, non-parametric tests such as the Mann–Whitney U test or Kruskal–Wallis test were employed. For time-dependent in vivo experiments, repeated measures ANOVA was used to evaluate the effect of time. All statistical tests were two-tailed, with $p < 0.05$ considered statistically significant.

Results

SIRT1 promotes M2 macrophage polarization inducing HCC Post-CHB

We used 6-8-week-old C57BL/6 transgenic mice that specifically express HBV genes. RNA-seq was performed on liver tissues from two groups of mice. Differential expression analysis identified 496 DEGs, with 199 significantly downregulated and 297 significantly upregulated. The most notable gene was SIRT1 (Fig. 1A).

In the CHB group, impaired function of various immune regulatory cells was detected. Using the "CIBERSORT" method, we assessed immune cell infiltration in both groups. The results indicated a significant decrease in M1 macrophages and a significant increase in M2 macrophages in the CHB group (Fig. 1B).

A heatmap was used to show the expression of genes related to M2 polarization, including ARG1, MRC1 (CD206), CCL22, and IL10, all of which were highly expressed in the CHB group. In contrast, M1 macrophage-related genes such as NOS2, IL-1β, TNF-α, IL-6, CXCL10, and IFN-γ were downregulated in the CHB group (Fig. 1C).

Functional enrichment analysis of 486 DEGs revealed significant enrichment in the PI3K-Akt signaling pathway, FoxO signaling pathway, IL-17 signaling pathway, and NF-kappa B signaling pathway according to KEGG results (Fig. 1D). GO analysis showed significant associations in BP with organic hydroxy compound metabolic process, regulation of lipid metabolic process, and organic hydroxy compound biosynthetic process (Fig. 1E); in cellular component (CC) with plasma membrane part, cell surface, and side of the membrane (Fig. 1F); and in molecular function (MF) with signaling receptor binding, cytokine receptor binding, and CCR chemokine receptor binding (Fig. 1G).

The proteomic differential analysis identified 22 DEPs, with 6 significantly downregulated and 16 significantly upregulated. SIRT1 was the most significantly altered, with ARG1 and IL10 significantly downregulated and TNF and IL-6 significantly upregulated (Fig. 2A-B).

Functional enrichment analysis of DEPs revealed significant enrichment in the PI3K-Akt signaling pathway, FoxO signaling pathway, IL-17 signaling pathway, and AGE-RAGE signaling pathway in diabetic complications according to KEGG results (Fig. 2C). GO analysis showed significant associations in BP with response to oxygen-containing compounds, cellular response to oxygen-containing compounds, and response to hormones (Fig. 2D); in CC with transferase complex, phosphatidylinositol 3-kinase complex, class I, and interleukin-6 receptor complex (Fig. 2E); and in MF with molecular function (MF) regulator, cytokine receptor binding, and receptor-ligand activity (Fig. 2F).

Overall, SIRT1 was the most significantly altered gene in both the transcriptome and proteome. Previous studies have reported that SIRT1 plays a role in regulating inflammation [49] and can promote the progression of various cancers [50, 51]. SIRT1 downregulates M1 macrophage markers and upregulates M2 macrophage markers [52]. In summary, we hypothesize that SIRT1 may induce HCC post-CHB by inhibiting M1 macrophage polarization and promoting M2 polarization.

Mesoporous silica nanoparticles exhibit excellent stability and drug release properties

By integrating the results from transcriptomics and proteomics sequencing analyses, we hypothesize that SIRT1 may induce the occurrence of liver cancer following chronic hepatitis B (CHB) by inhibiting M1 macrophage polarization and promoting M2 polarization. To further investigate the impact of SIRT1 on the development of liver cancer, we employed the SIRT1 inhibitor EX-527 for liver cancer treatment. To overcome issues such as the

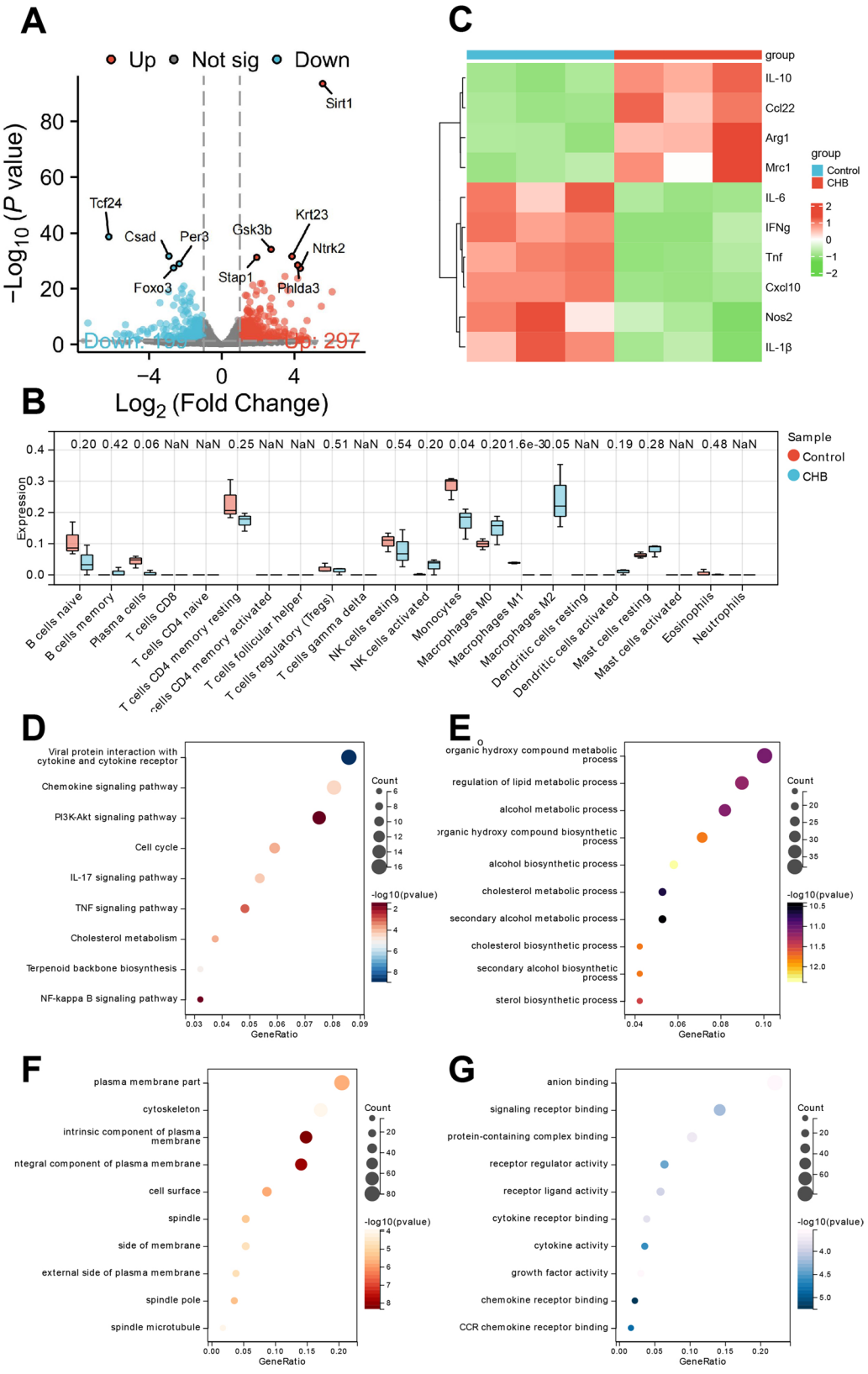

Fig. 1 Transcriptional Profiling Analysis of CHB Mouse Liver Tissue. Note: (**A**) Volcano plot of differential analysis of transcriptome sequencing, where red indicates significantly upregulated genes, blue indicates significantly downregulated genes, and gray represents genes with no significant difference; (**B**) Infiltration status of two immune cell groups; (**C**) Heatmap of marker genes for M1 and M2 macrophages; (**D**) KEGG enrichment analysis of DEGs; (**E**-**G**) GO enrichment analysis of DEGs, including BP (**E**), CC (**F**), and MF (**G**). Control: $n = 3$; CHB: $n = 3$

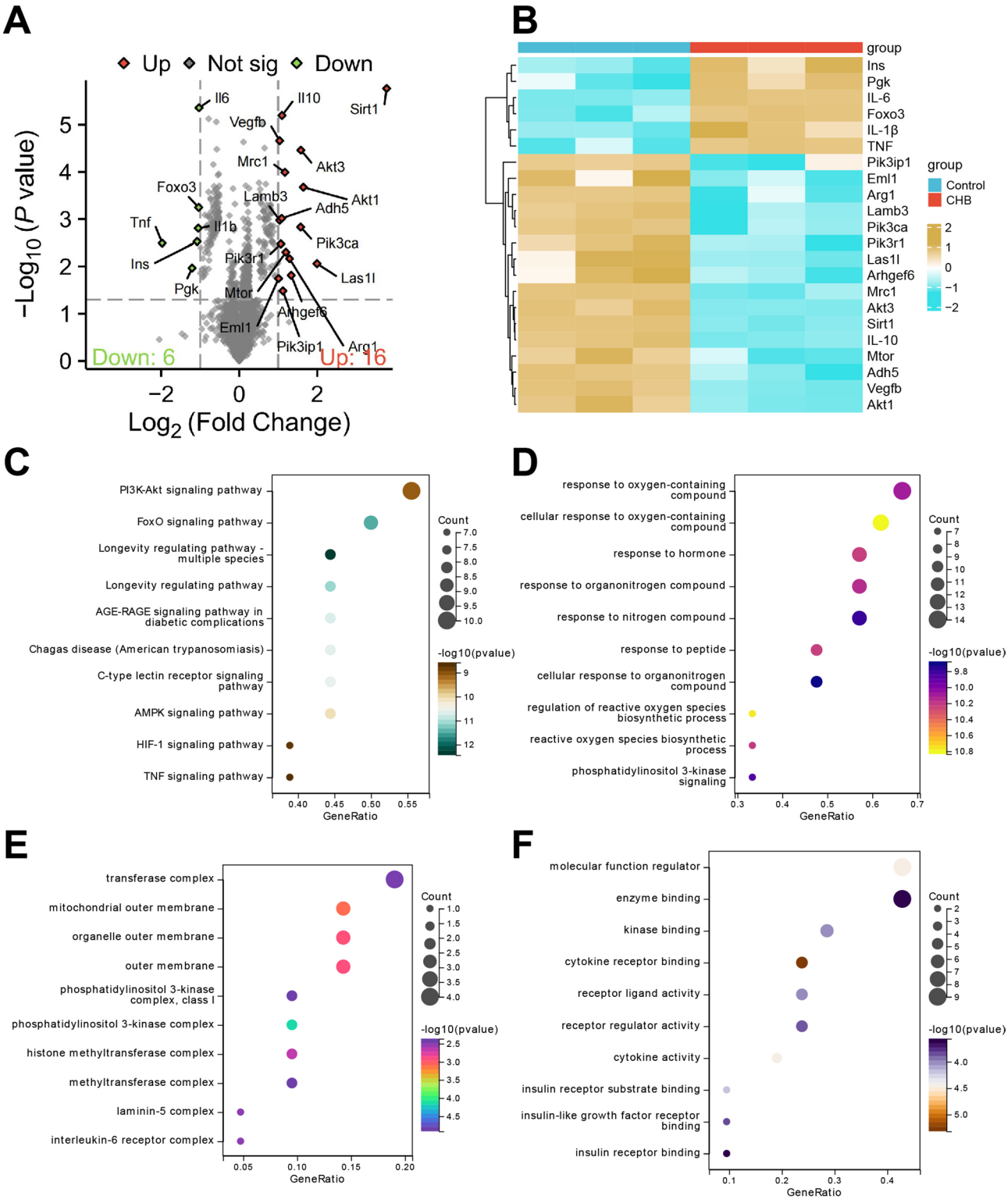

Fig. 2 Proteomic Analysis of Mouse Liver Tissue in CHB Mice. Note: (**A**) Volcano plot of proteomic differential analysis, where red indicates significantly upregulated proteins, green indicates significantly downregulated proteins, and grey represents proteins with no significant difference; (**B**) Heat map of DEPs; (**C**) KEGG enrichment analysis of DEPs; (**D**-**F**) GO analysis of DEPs, BP (**D**), CC (**E**), MF (**F**). Control group: $n=3$; CHB group: $n=3$

short half-life and lack of target specificity of the drug, we designed a mesoporous silica nanoparticle-based targeted delivery system. This system utilizes mesoporous silica as the core, loading the inhibitor through covalent bonds into the drug, and targets specific receptors expressed in the liver, such as integrin αvβ3, through modifications with fibrinogen(PMID: 28340512和PMID: 15661807). This study aims to develop a new type of nanoparticle drug that has liver targeting, controlled release, and extended drug half-life capabilities (Fig. 3A).

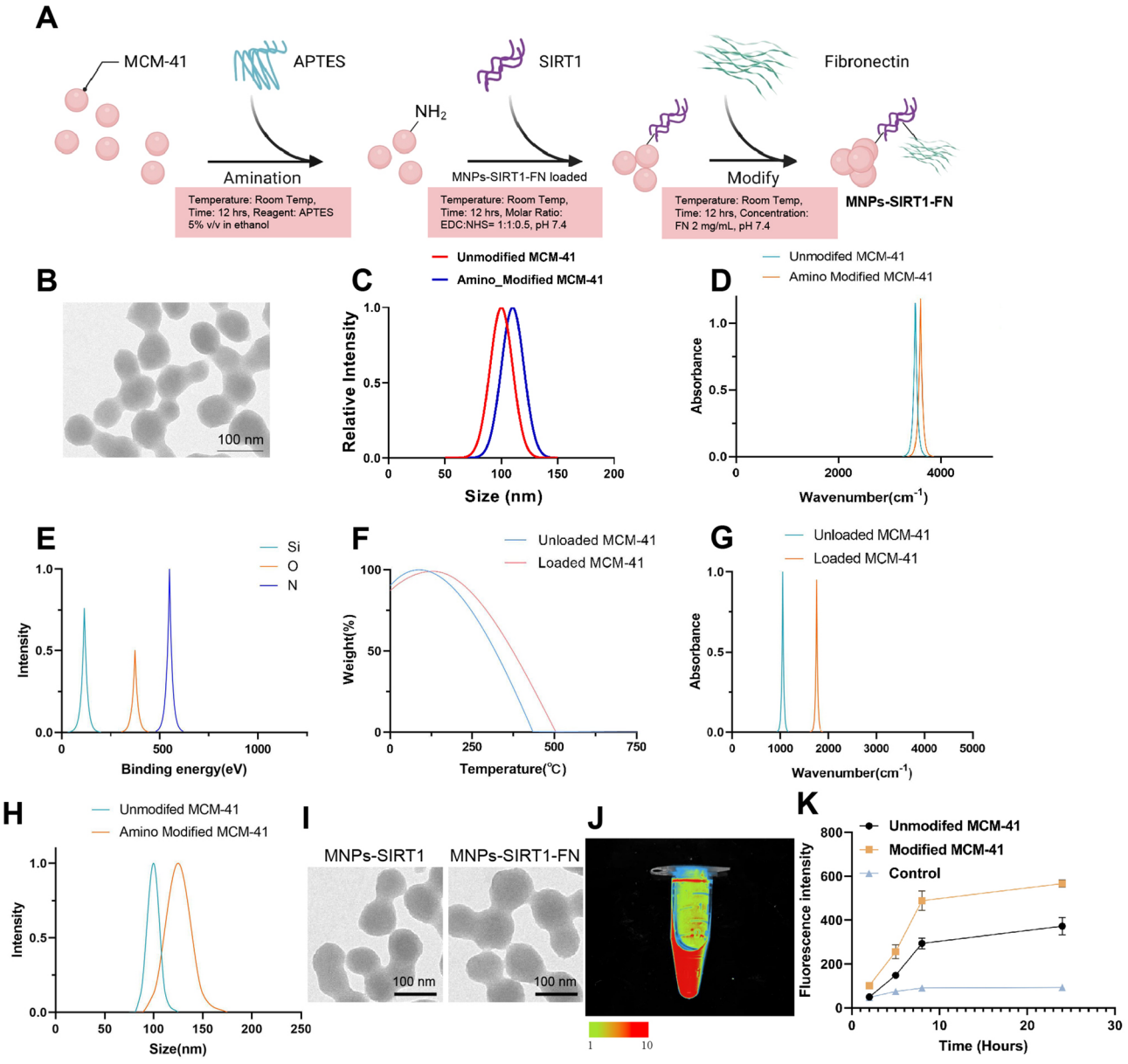

Fig. 3 Preparation and Characterization of MNPs. Note: (**A**) Schematic illustration of the preparation process of MNPs-SIRT1-FN (starting from the base MCM-41 nanoparticles, through amination modification, SIRT1 inhibitor loading, to fibronectin modification). (**B**) TEM image displaying the uniform spherical morphology of MCM-41 nanoparticles, with an average particle size of approximately 100 nanometers. (**C**) DLS results showcase the particle size distribution of modified nanoparticles, confirming a slight increase in size after surface modification. (**D**) FTIR spectra demonstrating characteristic absorption peaks of nanoparticles before and after amination modification, validating the success of chemical modification. (**E**) XPS analysis confirms the successful introduction of amines onto the nanoparticle surface. (**F**) TGA results show the thermal stability of nanoparticles after SIRT1 inhibitor loading. (**G**) FTIR further confirms the successful loading of the SIRT1 inhibitor onto the nanoparticles. (**H**) DLS results indicate changes in particle size before and after fibronectin modification. (**I**) TEM images show the uniform spherical morphology of MNPs-SIRT1 and MNPs-SIRT1-FN. (**J**) A fluorescence microscopy image displays the fluorescence signal of FITC-labeled nanoparticles, confirming successful labeling. (**K**) FACS results reveal the cellular uptake of fluorescently labeled nanoparticles. All data are expressed as mean ± standard error, with each experiment repeated three times. Statistical analysis was conducted using ANOVA and Tukey's post-hoc test, where * indicates $p < 0.05$, ** indicates $p < 0.01$, and *** indicates $p < 0.001$

The MCM-41 nanoparticles, prepared via the sol-gel method, exhibited a uniform spherical morphology under TEM with an average particle size of approximately 100 nm (Fig. 3B). DLS results demonstrated a narrow size distribution, indicating good uniformity and dispersion (Fig. 3C). The MCM-41 nanoparticles were aminated using 3-aminopropyltriethoxysilane (APTES). FTIR showed a prominent N-H stretching vibration peak at 3400 cm^{-1}, confirming the introduction of amino groups (Fig. 3D). X-ray Photoelectron Spectroscopy (XPS) further verified the successful amination (Fig. 3E).

Using EDC/NHS coupling, the SIRT1 inhibitor EX-527 was successfully loaded onto the aminated nanoparticles. Thermogravimetric Analysis (TGA) indicated significant weight loss between 200 and 300 °C, suggesting a high loading of the SIRT1 inhibitor, with the modified nanoparticles maintaining good thermal stability below 300 °C (Fig. 3F). FTIR analysis also confirmed the successful binding of the SIRT1 inhibitor, as evidenced by the appearance of characteristic absorption peaks of the inhibitor (Fig. 3G). Furthermore, fibronectin (FN) was covalently attached to the nanoparticles loaded with the SIRT1 inhibitor via EDC/NHS coupling. FTIR and XPS analysis confirmed the presence of fibronectin's characteristic absorption peaks and elemental signals on the modified nanoparticles. DLS results showed an increase in particle size, indicating successful fibronectin modification (Fig. 3H).

TEM observations indicate that the modified nanoparticles maintain a spherical shape and uniform size distribution (Fig. 3I). DLS results demonstrate that the nanoparticles exhibit good dispersion in aqueous solution and possess a positive surface charge, indicating stability under physiological conditions. The nanoparticles

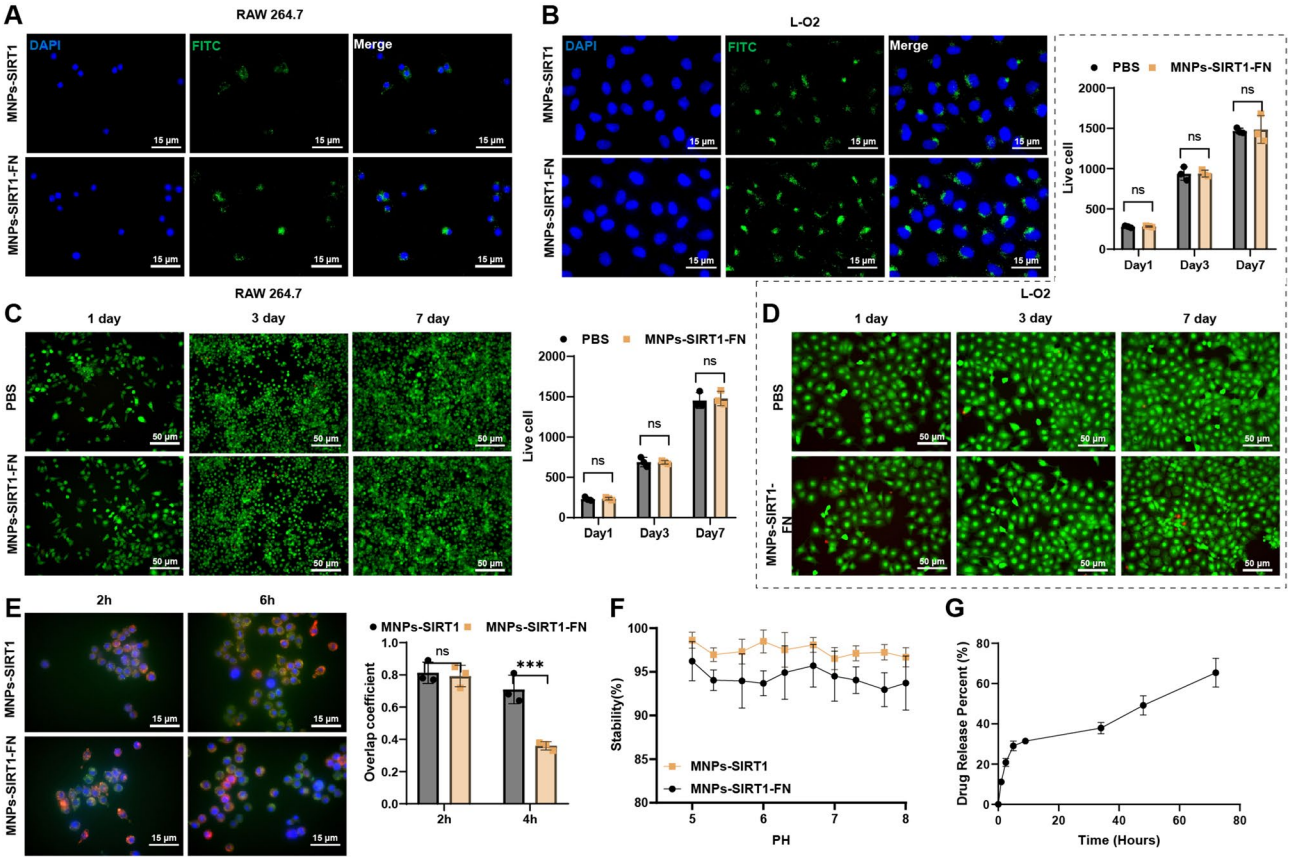

Fig. 4 Characterization of Multifunctional Biomimetic Nanoparticles. Note: (**A**-**B**) Confocal microscopy analysis of RAW 264.7 and L-O2 cells after 24 h of culture with MNPs-SIRT1 and MNPs-SIRT1-FN nanoparticles, showing nanoparticle uptake (scale bar = 10 μm). (**C**-**D**) Live/dead cell staining to assess the toxicity of MNPs-SIRT1-FN nanoparticles to RAW 264.7 and L-O2 cells, 'ns' indicates no significant difference compared to the PBS group (scale bar = 100 μm). (**E**) Lysosomal escape of nanoparticles assessed by CLSM after 2 h and 6 h of incubation, with blue fluorescence representing Hoechst 33,342 nuclear staining, green fluorescence representing Lyso-Tracker lysosomal staining, and red fluorescence representing RhB-labeled nanoparticles (scale bar = 50 μm). (**F**) Chemical stability testing results indicate that within the pH range of 5.0 to 8.0, the nanoparticles demonstrate excellent chemical stability. (**G**) Analysis of drug release properties reveals that nanoparticles loaded with SIRT1 inhibitors rapidly release approximately 40% of the drug under simulated physiological conditions in vitro within 24 h, followed by a gradual release over 72 h, demonstrating favorable sustained release characteristics that align with the requirements of long-term therapy. All data are expressed as mean ± standard error, with experiments repeated three times. Statistical analysis was conducted using ANOVA and Tukey post hoc tests, with * indicating $p < 0.05$, ** indicating $p < 0.01$, and *** indicating $p < 0.001$

were labeled with fluorescein isothiocyanate (FITC) and verified using fluorescence microscopy and flow cytometry. The results show that the labeled nanoparticles exhibit strong fluorescence signals under fluorescence microscopy (Fig. 3J). Flow cytometry results indicate significant cellular uptake of the fluorescently labeled nanoparticles, confirming successful labeling and good biocompatibility (Fig. 3K).

In addition, we performed immunofluorescence staining to examine the uptake of MNPs-SIRT1 and MNPs-SIRT1-FN nanoparticles by RAW 264.7 and L-O2 cells. Green fluorescence was observed in both cell types after co-incubation with MNPs-SIRT1 and MNPs-SIRT1-FN, indicating that both types of nanoparticles were successfully internalized by the cells. Notably, under equivalent dosages, MNPs-SIRT1-FN exhibited significantly higher cellular uptake than MNPs-SIRT1 (Fig. 4A-B), further confirming that fibronectin modification enhances nanoparticle uptake.

We further evaluated the biosafety of MNPs-SIRT1-FN nanoparticles. Live/dead cell staining showed that, compared to the PBS group, the nanoparticles exhibited negligible cytotoxicity to both L-O2 and macrophage cells (Fig. 4C-D). To investigate the lysosomal escape capability of the nanoparticles, RhB-labeled nanoparticles were co-incubated with RAW 264.7 cells and observed via CLSM. As shown in Fig. 4E, after 2 h of incubation, the red fluorescence from RhB-labeled MNPs-SIRT1 and MNPs-SIRT1-FN co-localized with green lysosomal fluorescence, forming yellow puncta. However, after 6 h, most of the red fluorescence in the MNPs-SIRT1-FN group was separated from the green signal, suggesting a successful escape from lysosomes. In contrast, the MNPs-SIRT1 group remained co-localized with lysosomes. These results indicate that immunoprotein modification promotes lysosomal escape, thereby enabling more nanoparticles to target SIRT1 (Fig. 4E).

Further chemical stability tests show that the nanoparticles maintain stability within a physiological pH range (pH 5.0–8.0), indicating their suitability for biomedical applications (Fig. 4F). The encapsulation efficiency (EE%) of the SIRT1 inhibitor in the nanoparticles was 67.56 ± 5.67%, and the drug loading (DL%) was 6.67 ± 0.83%. Both the encapsulation rate and drug loading of these nanoparticles are considered to be good. Under simulated physiological conditions, the drug release profile of SIRT1 inhibitor-loaded nanoparticles was tested in vitro (Fig. 4G). The results reveal that approximately 40% of the drug is released within the first 24 h, followed by a gradual release over the next 72 h, demonstrating good sustained-release properties. The release curve indicates that the nanoparticles can stably release the drug, meeting the requirements for long-term therapy.

MNPs delivering SIRT1 inhibitors significantly inhibit M2 macrophage polarization

The workflow for in vitro cell experiments is shown in Fig. 5A. In RAW 264.7, after 24 h of treatment with MNPs, the numbers of M1 and M2 macrophages were analyzed using flow cytometry at different nanoparticle concentrations(Fig. 5B). The results showed that the number of M1 macrophages in the nanoparticle-treated groups was significantly higher than in the control group ($p < 0.05$), while the number of M2 macrophages was significantly lower than in the control group ($p < 0.05$). Furthermore, as the concentration of nanoparticles increased, the number of M1 macrophages gradually increased, whereas the number of M2 macrophages gradually decreased, resulting in a progressively higher ratio of M1 to M2 macrophages (Fig. 5C-F).

Flow cytometry analysis revealed that the expression of M2 macrophage markers CD206 and Arg1 was significantly lower in the nanoparticle-treated groups compared to the control group ($p < 0.05$). In the low concentration group (10 μg/mL), the proportion of CD206-positive cells decreased by approximately 30%, and Arg1-positive cells decreased by about 27%. In the medium concentration group (50 μg/mL), CD206-positive cells decreased by approximately 41%, and Arg1-positive cells decreased by about 34%. In the high concentration group (100 μg/mL), CD206-positive cells decreased by approximately 67%, and Arg1-positive cells significantly decreased by about 57% (Fig. 5G). Previous studies have shown that SIRT1 may be negatively correlated with IL-10/TGF-β levels through the NF-κB pathway [53, 54]. ELISA results showed that the secretion levels of anti-inflammatory cytokines IL-10 and TGF-β in the treated groups significantly increased with the concentration of nanoparticles ($p < 0.05$). In the low concentration group (10 μg/mL), IL-10 secretion increased by approximately 1.5 times, and TGF-β secretion increased by about 1.4 times. In the medium concentration group (50 μg/mL), IL-10 secretion increased by approximately 2 times, and TGF-β secretion increased by about 1.8 times. In the high concentration group (100 μg/mL), IL-10 secretion increased by approximately 3 times, and TGF-β secretion significantly increased by about 2.5 times (Fig. 5H).

RT-qPCR results showed significant changes in the expression levels of the SIRT1 gene in different nanoparticle treatment groups relative to the housekeeping gene GAPDH ($p < 0.05$). Specifically, the relative expression of the SIRT1 gene decreased by approximately 30% in the low concentration (10 μg/mL) treatment group, by about 45% in the medium concentration (50 μg/mL) treatment group, and by roughly 75% in the high concentration (100 μg/mL) treatment group (Fig. 5I). These changes were further validated by Western Blot analysis, which demonstrated significant alterations in the expression

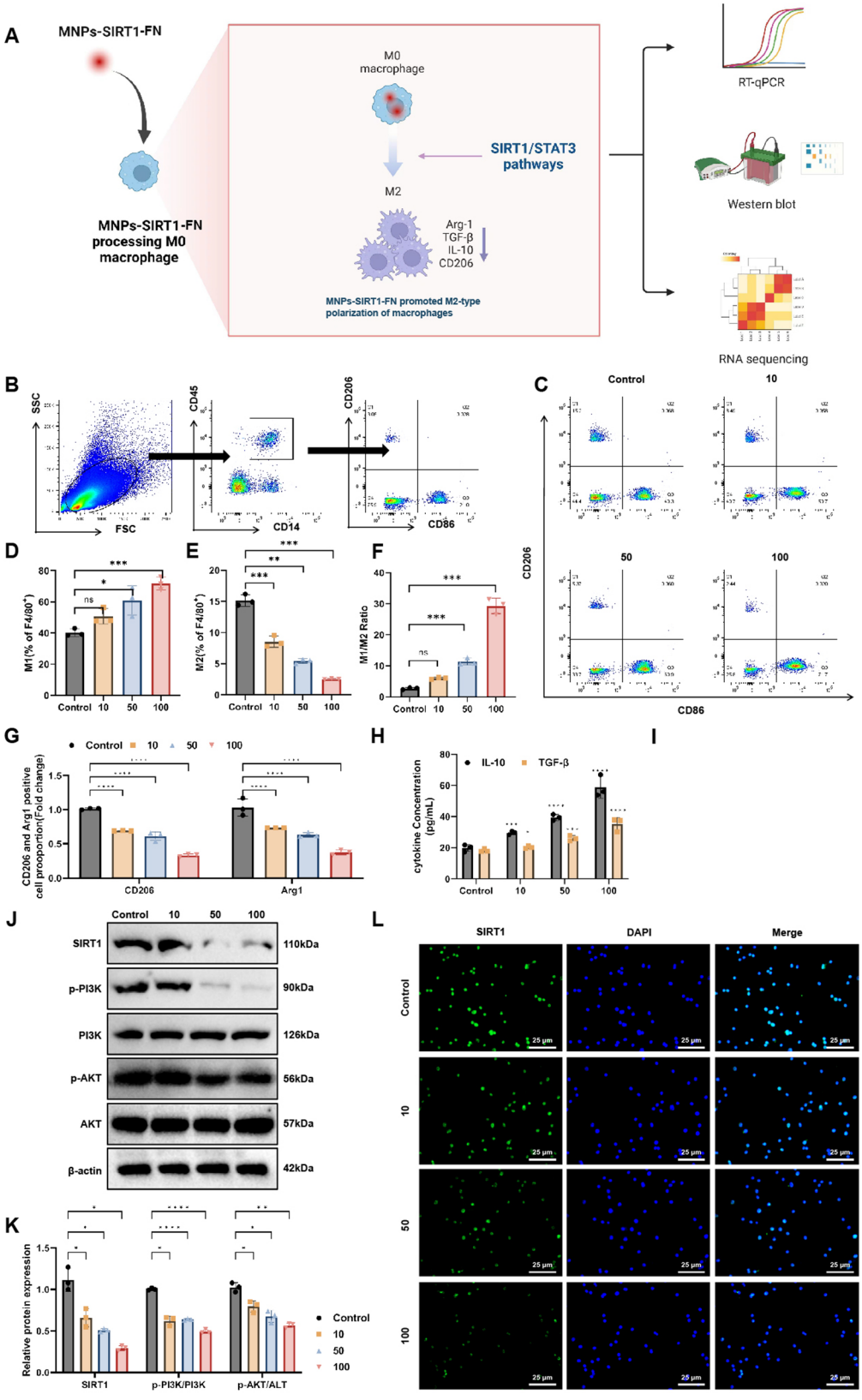

Fig. 5 (See legend on next page.)

(See figure on previous page.)

Fig. 5 MNPs Delivery of SIRT1 Inhibitor Inhibits Macrophage M2 Polarization by Regulating the SIRT1/PI3K-AKT Signaling Pathway. Note: (**A**) Schematic of in vitro cell experiment process. (**B**) Flow cytometry gating strategy for M1 and M2 macrophages. (**C**) Flow cytometry analysis of the ratio of M1 to M2 macrophages after treatment with different concentrations of nanoparticles. (**D**) Statistical chart of the M1 macrophage ratio. (**E**) Statistical chart of the M1 macrophage ratio. (**F**) The ratio of M1 macrophages to M2 macrophages. (**G**) Expression levels of M2 polarization markers CD206 and Arg1 in macrophages after treatment with different concentrations of nanoparticles. (**H**) Impact of different nanoparticle concentrations on the secretion of Anti-inflammatory Cytokines IL-10 and TGF-β in RAW 264.7 cells. (**I**) Influence of different nanoparticle concentrations on the gene expression of SIRT1 in RAW 264.7 cells. (**J**) Effects of different nanoparticle concentrations on the protein expression of SIRT1, p-PI3K/PI3K, and p-AKT/AKT in RAW 264.7 cells using Western Blot analysis. (**K**) Quantitative analysis of SIRT1, p-PI3K/PI3K, and p-AKT/AKT protein expression in RAW 264.7 cells. (**L**) Immunofluorescence staining results showed reduced nuclear localization of SIRT1 (green) in different nanoparticle treatment groups (scale bar: 25 μm). All data are presented as mean ± standard error, the experiments were repeated three times, and statistical analysis was performed using ANOVA and Tukey post hoc test; * indicates $p < 0.05$, ** indicates $p < 0.01$, *** indicates $p < 0.001$, **** indicates $p < 0.0001$

levels of SIRT1, p-PI3K, and p-AKT/AKT proteins across different nanoparticle concentrations ($p < 0.05$). Specifically, SIRT1 protein levels decreased by about 30% in the low concentration (10 μg/mL) group, by approximately 50% in the medium concentration (50 μg/mL) group, and by around 70% in the high concentration (100 μg/mL) group. Conversely, p-PI3K/PI3K and p-AKT/AKT protein levels decreased by approximately 30% and 20%, respectively, in the low-concentration group, by about 40% and 30% in the medium-concentration group and increased by roughly 50% and 42% in the high concentration group (Fig. 5J-K). The expression of the housekeeping protein β-actin remained stable across all treatment groups, indicating consistent protein loading. These findings suggest that nanoparticle treatments significantly regulate SIRT1 protein expression in RAW 264.7 in a concentration-dependent manner. Immunofluorescence staining revealed reduced nuclear localization of SIRT1 in the different nanoparticle treatment groups (Fig. 5L). These results indicate a significant change in SIRT1 localization within the cell following nanoparticle treatment, implying alterations in the activation state of the SIRT1/PI3K-AKT signaling pathway, thereby promoting M2 macrophage polarization.

Distribution and clearance dynamics of MNPs in mice

The distribution of MNPs in mice was tracked using fluorescent labeling. Results indicated that within 3 h post-injection, the MNPs rapidly accumulated in the liver (Fig. 6A), reaching their peak concentration at 24 h. The targeting of nanoparticles to the liver was significantly improved with fibronectin modification compared to nanoparticles without fibronectin modification, especially at 24 h post-injection. Subsequently, the fluorescent signal gradually diminished, and by 72 h, a significantly reduced level of fluorescence was observed in the liver (Fig. 6B).

Additionally, 24 h after the injection of the nanoparticles, the mice were euthanized and their major organs (heart, liver, spleen, lungs, kidneys, and brain) were collected for ex vivo imaging analysis. The results indicated a significant increase in the distribution of the fibrinogen-modified multifunctional biomimetic nanoparticles in the mouse liver (Fig. 6C-D). This finding suggests that the modification with fibrinogen effectively enhances the liver-targeting ability of the nanoparticles.

MNPs delivering SIRT1 inhibitors significantly inhibit macrophage M2 polarization in mice

Flow cytometry analysis (Fig. 7A-B) demonstrated a significant increase in the expression of M1 macrophage markers (CD80 and CD86) in the treatment group compared to the control group ($p < 0.05$). Conversely, the expression of the M2 macrophage marker (CD206) was significantly decreased in the treatment group, showing a statistically significant difference from the control group ($p < 0.05$). Flow cytometry assay showed a significant increase in the number of M1 macrophages and a significant decrease in the number of M2 macrophages compared to the control group, demonstrating the potential immunomodulatory effect of SIRT1 inhibitor (Fig. 7C-D). These findings indicate that SIRT1 inhibitors delivered through a nanoparticle system can effectively modulate macrophage polarization, promoting a shift in the immune microenvironment from an anti-inflammatory to a pro-inflammatory state.

MNPs delivering SIRT1 inhibitors significantly improve liver pathology and function in mice

Histological examination using H&E staining (Fig. 8A) revealed that the liver tissues in the treatment group displayed clear hepatocyte boundaries, significantly reduced infiltration of inflammatory cells, and marked improvement in liver fibrosis. Immunohistochemical analysis (Fig. 8B) further demonstrated a significant reduction in SIRT1 expression in the liver tissues of the treatment group compared to the control group. In addition, immunofluorescence staining showed that compared with the Control group, the expression of CD206 protein in the liver tissues of mice in the Treatment group was significantly reduced, whereas the expression of F4/80 and CD80 proteins was significantly increased, which indicated that the number of macrophages in the liver tissues of mice was significantly increased by the action of the nanoparticles, and that the nanoparticles promoted the M1 polarisation of the macrophages and suppressed the

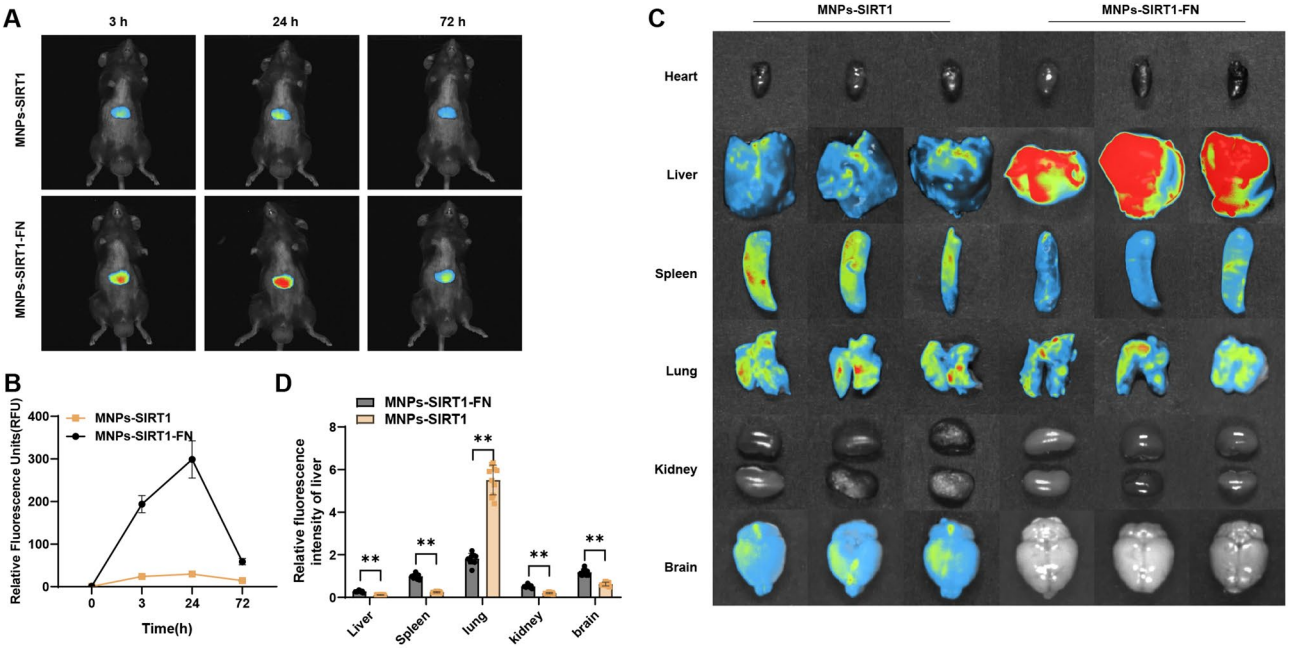

Fig. 6 Distribution Dynamics and Metabolic Process of MNPs in Mice. Note: (**A**) Fluorescence imaging: Fluorescence imaging results of MNPs in the livers of mice at different time points (3 h, 24 h, and 72 h) after injection. (**B**) Time course of fluorescence intensity in the liver. (**C**) Ex vivo imaging of the major organs (heart, liver, spleen, lungs, kidneys, and brain) in mice 24 h after injection of the multifunctional biomimetic nanoparticles. (**D**) Statistical chart of the quantitative fluorescence intensity in the liver

macrophage M2 polarisation (Fig. 8C-D). These changes are closely associated with improvements in liver pathology, indicating that MNPs delivering SIRT1 inhibitors exert a significant therapeutic effect.

Post-treatment, as shown in Fig. 8E, the levels of serum ALT and AST in the treatment group were significantly lower than those in the control group, with ALT levels reduced by 45% and AST levels by 38%, both changes being statistically significant ($p < 0.01$). The substantial improvement in these biochemical markers suggests that SIRT1 inhibitors can effectively alleviate liver inflammation and cellular damage, thereby protecting liver function.

Finally, we conducted an in vivo biosafety assessment of the multifunctional biomimetic nanoparticles. The results showed that no significant damage was observed in the heart, brain, spleen, lung, and kidney tissues of the mice across all groups, as evidenced by H&E staining (Figure S2). This indicates that the nanoparticles possess good biosafety.

Discussion

This study aims to investigate the delivery of SIRT1 inhibitors using MNPs to modulate Macrophage M2 Polarization, thereby reshaping the liver immune microenvironment and preventing the progression of HCC following CHB. Compared to previous studies, this research demonstrates significant innovations in both techniques and methodology. Traditional studies often focus on the mechanisms of single molecules. In contrast, this study employs nanoparticle delivery to enhance the efficacy of SIRT1 inhibitors in reaching target cells and modulates macrophage polarization to comprehensively reshape the liver immune microenvironment. This strategy not only improves the targeting and stability of the drug but also reduces its side effects, highlighting its potential for clinical applications.

For the experimental design, we utilized 6-8-week-old C57BL/6 transgenic mice specifically expressing HBV genes to establish an animal model of CHB. This approach more accurately simulates the pathological process of human CHB than previous methods. Through RNA and proteomic analyses of liver tissues from both control and CHB groups, we identified various DEGs and DEPs associated with the development of HCC. High-throughput RNA-seq and proteomic analysis not only enhanced the comprehensiveness and accuracy of the data but also deepened our understanding of the role of SIRT1 in HCC post-CHB, providing a solid foundation for future research.

One of the primary findings of this study is the significant upregulation of SIRT1 expression in the liver tissues of CHB mice. Immunohistochemical analysis revealed a notable decrease in M1 macrophages and a corresponding increase in M2 macrophages in the CHB group. This observation aligns with previous studies and further substantiates the critical role of SIRT1 in regulating immune cell polarization. Genes associated with M2 polarization,

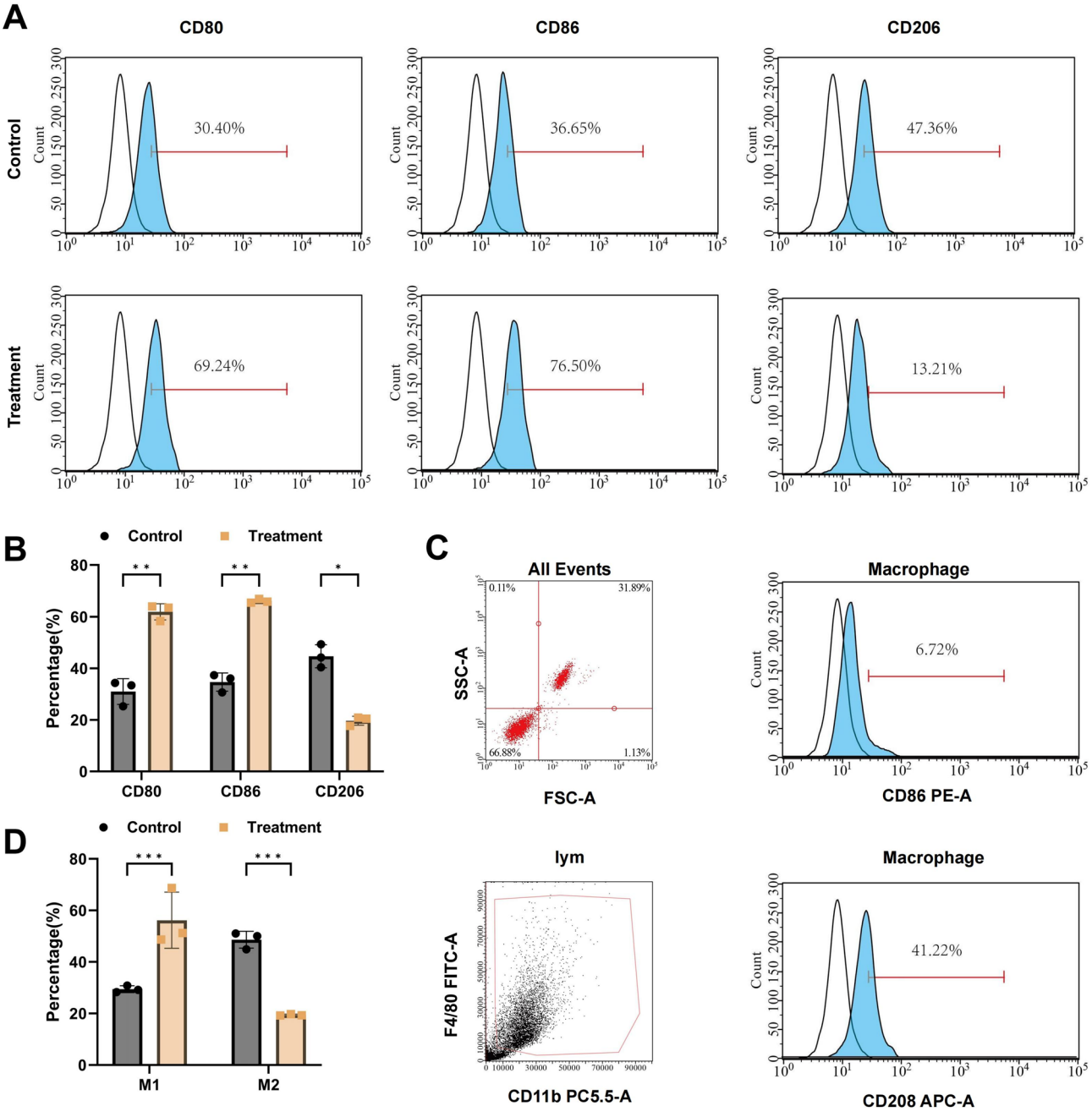

Fig. 7 Regulation of Macrophage Polarization in Mice by Delivery of SIRT1 Inhibitor Using MNPs. Notes: (**A**-**B**) Expression levels of M1 macrophage markers CD80 and CD86 and M2 macrophage marker CD206 in the treatment and control groups; (**C**) Flow cytometry gating strategy for M1 and M2 macrophages; (**D**) Ratio of M1 to M2 macrophages. All data are presented as mean ± standard error, the experiments were repeated three times, and statistical analysis was performed using Student's t test; ** indicates $p < 0.01$, **** indicates $p < 0.0001$

such as ARG1, MRC1, CCL22, and IL10, were upregulated in the HBV group, whereas genes linked to M1 polarization, including NOS2, IL-1β, and TNF-α, were downregulated [55]. These results suggest that SIRT1 influences the hepatic immune microenvironment in CHB by modulating macrophage polarization, which may play a pivotal role in the development of HCC.

Additionally, this study identified several key signaling pathways related to liver pathology, such as PI3K-Akt, FoxO, IL-17, and NF-kappa B, through the screening of DEGs and DEPs. Functional enrichment analysis further confirmed the potential involvement of these pathways in liver lesions induced by HBV infection. Proteomics analysis also indicated a strong association between SIRT1 activity and the PI3K-Akt signaling pathway, suggesting

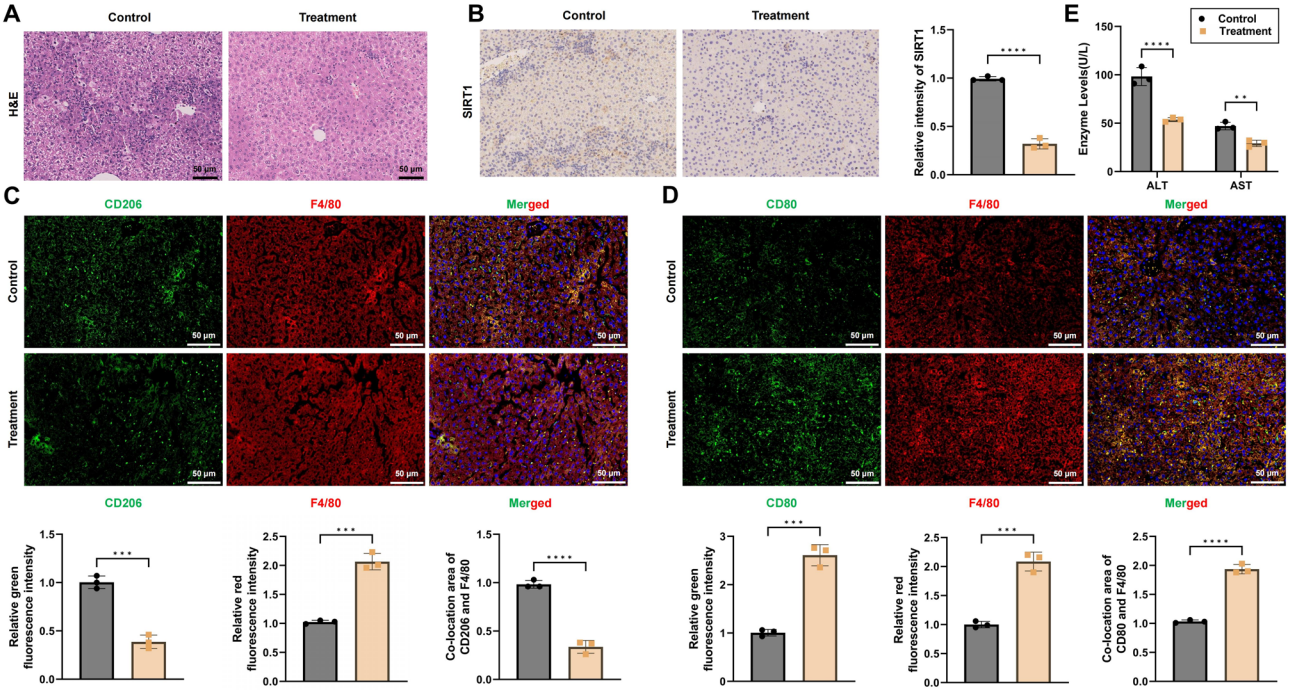

Fig. 8 Impact of MNPs Delivery of SIRT1 Inhibitor on the Hepatic Pathological Structure in Mice. Note: (**A**) H&E staining of mouse liver tissue. (**B**) Immunohistochemical staining images of liver tissue sections for SIRT1. (**C**-**D**) Immunofluorescence staining images of liver tissue sections for F4/80, CD206 and CD80. (**E**) Changes in serum ALT and AST levels before and after treatment. All data are presented as mean ± standard error, the experiments were repeated three times, and statistical analysis was performed using Student's t test; * indicates $p < 0.05$, ** indicates $p < 0.01$, *** indicates $p < 0.001$, **** indicates $p < 0.0001$

that SIRT1 may impact immune cell polarization by regulating this pathway, thereby contributing to the development of HCC post-CHB. These findings not only enhance our understanding of the mechanisms underlying HCC development post-CHB but also provide new perspectives for future therapeutic strategies.

The preparation and characterization of MNPs is a significant highlight of this study. We successfully synthesized MNPs loaded with a SIRT1 inhibitor and confirmed their structure and function through comprehensive characterization. Compared to traditional delivery systems, these MNPs exhibit enhanced stability and biocompatibility, allowing for more efficient delivery of the SIRT1 inhibitor. This study is the first to demonstrate that MNPs-SIRT1-FN can significantly inhibit macrophage M2 polarization. This finding not only confirms the advantages of nanoparticles in drug delivery but also offers new possibilities for the prevention and treatment of HCC.

In animal experiments, we found that the proportion of M2-type macrophages in the liver of mice in the treatment group was significantly reduced compared to the control group. Immune microenvironment analysis revealed an increased proportion of pro-inflammatory immune cells and a decreased proportion of immunosuppressive cells in the liver tissues of the treated mice, indicating an effective remodeling of the immune microenvironment. These results provide clearer evidence of the potential of SIRT1 inhibitors in HCC prevention compared to previous studies. This discovery not only enhances our understanding of the role of the immune microenvironment in HCC development but also offers new directions for future clinical applications.

In conclusion, our study demonstrates that MNPs delivering SIRT1 inhibitors can effectively regulate macrophage M2 polarization and remodel the liver immune microenvironment, thereby inhibiting the development and progression of HCC following CHB. This strategy holds significant value in scientific research and has promising clinical applications, providing new methods and insights for the prevention and treatment of HCC. However, this study has some limitations, such as being conducted only in a mouse model; further validation is needed to determine applicability to humans. Additionally, the long-term safety and biocompatibility of MNPs require further investigation. Future research should explore the application of SIRT1 inhibitors in other types of HCC and their combined use with other treatments. By continually optimizing nanoparticle delivery systems, we hope to provide more effective solutions for the comprehensive treatment of HCC.

Abbreviations

MNPs	Mimetic Nanoparticles
CHB	Chronic Hepatitis B

HCC	Hepatocellular Carcinoma
DEGs	Differentially Expressed Genes
DEPs	Differentially Expressed Proteins
DLS	Dynamic Light Scattering
TEM	Transmission Electron Microscopy
FTIR	Fourier Transform Infrared Spectroscopy
CLSM	Confocal Laser Scanning Microscopy
RAW 264.7	Bone marrow-derived macrophages
SIRT1	Sirtuin 1
RNA-seq	RNA Sequencing
KEGG	Kyoto Encyclopedia of Genes and Genomes
GO	Gene Ontology
H&E	Hematoxylin and Eosin
RT-qPCR	Real-Time Quantitative PCR
HBV	hepatitis B virus
SPF	specific pathogen-free
APTES	3-aminopropyltriethoxysilane
EDC	1-ethyl-3-(3-dimethylaminopropyl) carbodiimide
NHS	N-hydroxysuccinimide
FN	fibronectin
DMSO	dimethyl sulfoxide
PBS	phosphate-buffered saline
BP	Biological Process
CC	Cellular Component
MF	Molecular Function

Supplementary Information

The online version contains supplementary material available at https://doi.org/10.1186/s12951-025-03447-2.

Supplementary Material 1: Figure S1. Schematic Illustration of In Vivo Animal Experiment Procedure

Supplementary Material 2: Figure S2. In Vivo Biosafety Assessment of Multifunctional Biomimetic Nanoparticles

Acknowledgements
None.

Author contributions
He Zhang, Feng Yuan, Nan Zhao, and Wenqiang Tang contributed equally to the conceptualization, experimental design, data acquisition, and analysis. Pengwei Zhao and Chunfa Liu assisted with in vitro and in vivo experiments and data interpretation. Shan Chen and Xiaolin Hou supervised the study and contributed to manuscript preparation. Changyou Xia led the nanoparticle synthesis and characterization. Jun Chu provided project administration, funding acquisition, and final manuscript revision. All authors reviewed and approved the final manuscript.

Funding
This study was supported by Beijing University of Agricultural for Young Teachers' Research and Innovation Ability Improvement Plan: QJKC2022025; Open scientific research project of China Animal Husbandry Corporation: (2002)00905; National Natural Science Foundation of China (NSFC): 32072898; National Key R&D Program of China: 2023YFF0724604; Heilongjiang Province natural fund joint guidance project: LH2024C059.

Data availability
Data AvailabilityAll data generated or analyzed during this study are included in this article and/or its supplementary material files. Further enquiries can be directed to the corresponding author.

Declarations

Ethics approval and consent to participate
All animal experiments were approved by the Animal Ethics Committee of Beijing University of Agriculture (No. BUA812403010).

Consent for publication
Not applicable.

Competing interests
The authors declare no competing interests.

Author details
[1]College of Animal Science and Technology, Beijing University of Agriculture, No. 7 Beinong Road, Beijing 102206, China
[2]State Key Laboratory for Animal Disease Control and Prevention, Harbin Veterinary Research Institute, Chinese Academy of Agricultural Sciences, Harbin 150001, China
[3]Laboratory of Inflammation and Vaccines, Shenzhen Institutes of Advanced Technology, Chinese Academy of Sciences, Shenzhen 518055, China
[4]Institute of Clinical Medicine, National Infrastructures for Translational Medicine, Peking Union Medical College Hospital, Chinese Academy of Medical Science and Peking Union Medical College, Beijing 100730, China
[5]Institute of Animal Science, Tibet Academy of Agricultural and Animal Husbandry Science, Lhasa 850009, China
[6]The Fourth Affiliated Hospital, Zhejiang University School of Medicine, Yiwu 322000, China

Received: 4 February 2025 / Accepted: 5 May 2025
Published online: 27 May 2025

References

1. Rumgay H, Arnold M, Ferlay J, Lesi O, Cabasag CJ, Vignat J et al. Global burden of primary liver cancer in 2020 and predictions to 2040 [Internet]. Journal of Hepatology. Elsevier BV; 2022 [cited 2025 Apr 11]. pp. 1598–606. Available from: https://doi.org/10.1016/j.jhep.2022.08.021
2. Asafo-Agyei KO, Samant H. Hepatocellular carcinoma. StatPearls. Treasure Island (FL): StatPearls Publishing; 2023.
3. Lee H-Y, Nga HT, Tian J, Yi H-S. Mitochondrial Metabolic Signatures in Hepatocellular Carcinoma [Internet]. Cells. MDPI AG; 2021 [cited 2025 Apr 11]. p. 1901. Available from: https://doi.org/10.3390/cells10081901
4. Xia Z, Zhang J, Chen W, Zhou H, Du D, Zhu K et al. Hepatitis B reactivation in cancer patients receiving immune checkpoint inhibitors: a systematic review and meta-analysis [Internet]. Infect Dis Poverty. Springer Science and Business Media LLC; 2023 [cited 2025 Apr 11]. Available from: https://doi.org/10.1186/s40249-023-01128-6
5. Tian F, Feld JJ, Feng Z, Sander B, Wong WWL. Feasibility of hepatitis B elimination in high-income countries with ongoing immigration [Internet]. Journal of Hepatology. Elsevier BV; 2022 [cited 2025 Apr 11]. pp. 947–56. Available from: https://doi.org/10.1016/j.jhep.2022.04.014
6. Jeng W-J, Papatheodoridis GV, Lok ASF, Hepatitis B [Internet]. The Lancet., Elsevier BV. 2023 [cited 2025 Apr 11]. pp. 1039–52. Available from: https://doi.org/10.1016/s0140-6736(22)01468-4
7. Lee HW, Lee JS, Ahn SH, Hepatitis B. Virus Cure: Targets and Future Therapies [Internet]. IJMS. MDPI AG; 2020 [cited 2025 Apr 11]. p. 213. Available from: https://doi.org/10.3390/ijms22010213
8. Chien R-N, Liaw Y-F. Current Trend in Antiviral Therapy for Chronic Hepatitis B [Internet]. Viruses. MDPI AG; 2022 [cited 2025 Apr 11]. p. 434. Available from: https://doi.org/10.3390/v14020434
9. Khanam A, Chua JV, Kottilil S. Immunopathology of Chronic Hepatitis B Infection: Role of Innate and Adaptive Immune Response in Disease Progression [Internet]. IJMS. MDPI AG; 2021 [cited 2025 Apr 11]. p. 5497. Available from: https://doi.org/10.3390/ijms22115497
10. Jiang P, Jia H, Qian X, Tang T, Han Y, Zhang Z et al. Single-cell RNA sequencing reveals the immunoregulatory roles of PegIFN-α in patients with chronic hepatitis B [Internet]. Hepatology. Ovid Technologies (Wolters Kluwer Health); 2023 [cited 2025 Apr 11]. pp. 167–82. Available from: https://doi.org/10.1097/hep.0000000000000524
11. Loureiro D, Tout I, Narguet S, Bed CM, Roinard M, Sleiman A et al. Mitochondrial stress in advanced fibrosis and cirrhosis associated with chronic hepatitis B, chronic hepatitis C, or nonalcoholic steatohepatitis [Internet]. Hepatology. Ovid Technologies (Wolters Kluwer Health); 2022 [cited 2025 Apr 11]. pp. 1348–65. Available from: https://doi.org/10.1002/hep.32731

12. Roca Suarez AA, Testoni B, Zoulim FHBV. 2021: New therapeutic strategies against an old foe [Internet]. Liver International. Wiley; 2021 [cited 2025 Apr 11]. pp. 15–23. Available from: https://doi.org/10.1111/liv.14851
13. loading [Internet]. Available from: http://journal.yiigle.com/LinkIn.do?linkin_type=DOI&DOI=10.3760/cma.j.cn501113-20230316-00117
14. Luo X, He X, Zhang X, Zhao X, Zhang Y, Shi Y et al. Hepatocellular carcinoma: signaling pathways, targeted therapy, and immunotherapy [Internet]. MedComm. Wiley; 2024 [cited 2025 Apr 11]. Available from: https://doi.org/10.1002/mco2.474
15. Antonucci L, Canciani G, Mastronuzzi A, Carai A, Del Baldo G, Del Bufalo F. CAR-T Therapy for Pediatric High-Grade Gliomas: Peculiarities, Current Investigations and Future Strategies [Internet]. Front. Immunol. Frontiers Media SA; 2022 [cited 2025 Apr 11]. Available from: https://doi.org/10.3389/fimmu.2022.867154
16. Pang N, Shi J, Qin L, Chen A, Tang Y, Yang H et al. IL-7 and CCL19-secreting CAR-T cell therapy for tumors with positive glypican-3 or mesothelin [Internet]. J Hematol Oncol. Springer Science and Business Media LLC; 2021 [cited 2025 Apr 11]. Available from: https://doi.org/10.1186/s13045-021-01128-9
17. Kong F-H, Ye Q-F, Miao X-Y, Liu X, Huang S-Q, Xiong L et al. Current status of sorafenib nanoparticle delivery systems in the treatment of hepatocellular carcinoma [Internet]. Theranostics. Ivyspring International Publisher; 2021 [cited 2025 Apr 11]. pp. 5464–90. Available from: https://doi.org/10.7150/thno.54822
18. Yang R, Gao W, Wang Z, Jian H, Peng L, Yu X et al. Polyphyllin I induced ferroptosis to suppress the progression of hepatocellular carcinoma through activation of the mitochondrial dysfunction via Nrf2/HO-1/GPX4 axis [Internet]. Phytomedicine. Elsevier BV; 2024 [cited 2025 Apr 11]. p. 155135. Available from: https://doi.org/10.1016/j.phymed.2023.155135
19. Alawyia B, Constantinou C. Hepatocellular Carcinoma: a Narrative Review on Current Knowledge and Future Prospects [Internet]. Curr. Treat. Options in Oncol. Springer Science and Business Media LLC; 2023 [cited 2025 Apr 11]. pp. 711–24. Available from: https://doi.org/10.1007/s11864-023-01098-9
20. Di Benedetto F, Magistri P, Di Sandro S, Sposito C, Oberkofler C, Brandon E et al. Safety and Efficacy of Robotic vs Open Liver Resection for Hepatocellular Carcinoma [Internet]. JAMA Surg. American Medical Association (AMA); 2023 [cited 2025 Apr 11]. p. 46. Available from: https://doi.org/10.1001/jamasurg.2022.5697
21. Espírito Santo J, Ladeirinha A, Alarcão A, Strelet E, Reis M, Santos R et al. Hepatocellular carcinoma: tumor heterogeneity and recurrence after preoperative locoregional therapy [Internet]. Med Oncol. Springer Science and Business Media LLC; 2023 [cited 2025 Apr 11]. Available from: https://doi.org/10.1007/s12032-023-02208-1
22. Vogel A, Meyer T, Sapisochin G, Salem R, Saborowski A. Hepatocellular carcinoma [Internet]. The Lancet., Elsevier BV. 2022 [cited 2025 Apr 11]. pp. 1345–62. Available from: https://doi.org/10.1016/s0140-6736(22)01200-4
23. Chidambaranathan-Reghupaty S, Fisher PB, Sarkar D. Hepatocellular carcinoma (HCC): Epidemiology, etiology and molecular classification [Internet]. Advances in Cancer Research. Elsevier; 2021 [cited 2025 Apr 11]. pp. 1–61. Available from: https://doi.org/10.1016/bs.acr.2020.10.001
24. Brown ZJ, Tsilimigras DI, Ruff SM, Mohseni A, Kamel IR, Cloyd JM et al. Management of Hepatocellular Carcinoma [Internet]. JAMA Surg. American Medical Association (AMA); 2023 [cited 2025 Apr 11]. p. 410. Available from: https://doi.org/10.1001/jamasurg.2022.7989
25. Li J, Xuan S, Dong P, Xiang Z, Gao C, Li M et al. Immunotherapy of hepatocellular carcinoma: recent progress and new strategy [Internet]. Front. Immunol. Frontiers Media SA; 2023 [cited 2025 Apr 11]. Available from: https://doi.org/10.3389/fimmu.2023.1192506
26. Javed YS. Advanced therapeutics avenues in hepatocellular carcinoma: a novel paradigm [Internet]. Med Oncol. Springer Science and Business, Media LLC. 2023 [cited 2025 Apr 11]. Available from: https://doi.org/10.1007/s12032-023-02104-8
27. Eghbali S, Heumann TR. Next-Generation Immunotherapy for Hepatocellular Carcinoma: Mechanisms of Resistance and Novel Treatment Approaches [Internet]. Cancers. MDPI AG; 2025 [cited 2025 Apr 11]. p. 236. Available from: https://doi.org/10.3390/cancers17020236
28. Finn RS, Galle PR, Ducreux M, Cheng A-L, Reilly N, Nicholas A, Efficacy and Safety of Atezolizumab plus Bevacizumab versus Sorafenib in Hepatocellular Carcinoma with Main Trunk and/or Contralateral Portal Vein Invasion in IMbrave150 [Internet]. Liver Cancer., Karger S et al. AG; 2024 [cited 2025 Apr 11]. pp. 1–14. Available from: https://doi.org/10.1159/000539897
29. Finn RS, Qin S, Ikeda M, Galle PR, Ducreux M, Kim T-Y et al. Atezolizumab plus Bevacizumab in Unresectable Hepatocellular Carcinoma [Internet]. N Engl J Med. Massachusetts Medical Society; 2020 [cited 2025 Apr 11]. pp. 1894–905. Available from: https://doi.org/10.1056/nejmoa1915745
30. Vogel A, Meyer T, Saborowski A. IMbrave050: the first step towards adjuvant therapy in hepatocellular carcinoma [Internet]. The Lancet. Elsevier BV; 2023 [cited 2025 Apr 11]. pp. 1806–7. Available from: https://doi.org/10.1016/s0140-6736(23)01962-1
31. Crespo M, Nikolic I, Mora A, Rodríguez E, Leiva-Vega L, Pintor-Chocano A et al. Myeloid p38 activation maintains macrophage–liver crosstalk and BAT thermogenesis through IL-12–FGF21 axis [Internet]. Hepatology. Ovid Technologies (Wolters Kluwer Health); 2023 [cited 2025 Apr 11]. pp. 874–87. Available from: https://doi.org/10.1002/hep.32581
32. Ma C, Feng K, Yang X, Yang Z, Wang Z, Shang Y et al. Targeting macrophage liver X receptors by hydrogel-encapsulated T0901317 reduces atherosclerosis without effect on hepatic lipogenesis [Internet]. British J Pharmacology. Wiley; 2021 [cited 2025 Apr 11]. pp. 1620–38. Available from: https://doi.org/10.1111/bph.15387
33. Cheng P, Li S, Chen H. Macrophages in Lung Injury, Repair, and Fibrosis [Internet]. Cells. MDPI AG; 2021 [cited 2025 Apr 11]. p. 436. Available from: https://doi.org/10.3390/cells10020436
34. Wu H, Zheng J, Xu S, Fang Y, Wu Y, Zeng J et al. Mer regulates microglial/macrophage M1/M2 polarization and alleviates neuroinflammation following traumatic brain injury [Internet]. J Neuroinflammation. Springer Science and Business Media LLC; 2021 [cited 2025 Apr 11]. Available from: https://doi.org/10.1186/s12974-020-02041-7
35. Wu M-M, Wang Q-M, Huang B-Y, Mai C-T, Wang C-L, Wang T-T et al. Dioscin ameliorates murine ulcerative colitis by regulating macrophage polarization [Internet]. Pharmacological Research. Elsevier BV; 2021 [cited 2025 Apr 11]. p. 105796. Available from: https://doi.org/10.1016/j.phrs.2021.105796
36. Tu Y, Liu J, Kong D, Guo X, Li J, Long Z, Irisin drives macrophage anti-inflammatory differentiation via JAK2-STAT6-dependent activation of PPARγ and Nrf2 signaling [Internet]. Free Radical Biology and Medicine., Elsevier BV et al. 2023 [cited 2025 Apr 11]. pp. 98–110. Available from: https://doi.org/10.1016/j.freeradbiomed.2023.03.014
37. Wu H, Dong H, Tang Z, Chen Y, Liu Y, Wang M et al. Electrical stimulation of piezoelectric BaTiO3 coated Ti6Al4V scaffolds promotes anti-inflammatory polarization of macrophages and bone repair via MAPK/JNK inhibition and OXPHOS activation [Internet]. Biomaterials. Elsevier BV; 2023 [cited 2025 Apr 11]. p. 121990. Available from: https://doi.org/10.1016/j.biomaterials.2022.121990
38. Wang Y, Wang J, Gao R, Liu X, Feng Z, Zhang C et al. Biomimetic glycopeptide hydrogel coated PCL/nHA scaffold for enhanced cranial bone regeneration via macrophage M2 polarization-induced osteo-immunomodulation [Internet]. Biomaterials. Elsevier BV; 2022 [cited 2025 Apr 11]. p. 121538. Available from: https://doi.org/10.1016/j.biomaterials.2022.121538
39. Yang P, Qin H, Li Y, Xiao A, Zheng E, Zeng H et al. CD36-mediated metabolic crosstalk between tumor cells and macrophages affects liver metastasis [Internet]. Nat Commun. Springer Science and Business Media LLC; 2022 [cited 2025 Apr 11]. Available from: https://doi.org/10.1038/s41467-022-33349-y
40. Yu Z, Li Y, Li Y, Zhang J, Li M, Ji L et al. Bufalin stimulates antitumor immune response by driving tumor-infiltrating macrophage toward M1 phenotype in hepatocellular carcinoma [Internet]. J Immunother Cancer. BMJ; 2022 [cited 2025 Apr 11]. p. e004297. Available from: https://doi.org/10.1136/jitc-2021-004297
41. Ou D-L, Chen C-W, Hsu C-L, Chung C-H, Feng Z-R, Lee B-S et al. Regorafenib enhances antitumor immunity via inhibition of p38 kinase/Creb1/Klf4 axis in tumor-associated macrophages [Internet]. J Immunother Cancer. BMJ; 2021 [cited 2025 Apr 11]. p. e001657. Available from: https://doi.org/10.1136/jitc-2020-001657
42. Zou Y, Wang Y, Xu S, Liu Y, Yin J, Lovejoy DB et al. Brain Co-Delivery of Temozolomide and Cisplatin for Combinatorial Glioblastoma Chemotherapy [Internet]. Advanced Materials. Wiley; 2022 [cited 2025 Apr 11]. Available from: https://doi.org/10.1002/adma.202203958
43. Huang R-Y, Liu Z-H, Weng W-H, Chang C-W. Magnetic nanocomplexes for gene delivery applications [Internet]. J. Mater. Chem. B. Royal Society of Chemistry (RSC); 2021 [cited 2025 Apr 11]. pp. 4267–86. Available from: https://doi.org/10.1039/d0tb02713h
44. Hu L, Tao Y, Jiang Y, Qin F. Recent progress of nanomedicine in the treatment of Alzheimer's disease [Internet]. Front. Cell Dev. Biol. Frontiers Media SA; 2023 [cited 2025 Apr 11]. Available from: https://doi.org/10.3389/fcell.2023.1228679

45. Huang Y, Zhang C, Zhang L, Chen X, Fan W. Chemical Synthesis and Multihybridization of Small-Sized Hollow Mesoporous Organosilica Nanoparticles Toward Advanced Theranostics [Internet]. Acc. Chem. Res. American Chemical Society (ACS); 2024 [cited 2025 Apr 11]. pp. 3465–77. Available from: https://doi.org/10.1021/acs.accounts.4c00502
46. Kovtareva S, Kusepova L, Tazhkenova G, Mashan T, Bazarbaeva K, Kopishev E. Surface Modification of Mesoporous Silica Nanoparticles for Application in Targeted Delivery Systems of Antitumour Drugs [Internet]. Polymers. MDPI AG; 2024 [cited 2025 Apr 11]. p. 1105. Available from: https://doi.org/10.3390/polym16081105
47. Peck B, Chen C-Y, Ho K-K, Di Fruscia P, Myatt SS, Coombes RC et al. SIRT Inhibitors Induce Cell Death and p53 Acetylation through Targeting Both SIRT1 and SIRT2 [Internet]. Molecular Cancer Therapeutics. American Association for Cancer Research (AACR); 2010 [cited 2025 Apr 11]. pp. 844–55. Available from: https://doi.org/10.1158/1535-7163.mct-09-0971
48. GHATREH SAMANI K, FARROKHI E, TABATABAEE A, JALILIAN N. JAFARI M. Synergistic Effects of Lauryl Gallate and Tamoxifen on Human Breast Cancer Cell [Internet]. ijph. Knowledge E DMCC; 2020 [cited 2025 Apr 11]. Available from: https://doi.org/10.18502/ijph.v49i7.3586
49. Yang Y, Liu Y, Wang Y, Chao Y, Zhang J, Jia Y et al. Regulation of SIRT1 and Its Roles in Inflammation [Internet]. Front. Immunol. Frontiers Media SA; 2022 [cited 2025 Apr 11]. Available from: https://doi.org/10.3389/fimmu.2022.831168
50. Wei Z, Xia J, Li J, Cai J, Shan J, Zhang C et al. SIRT1 promotes glucolipid metabolic conversion to facilitate tumor development in colorectal carcinoma [Internet]. Int. J. Biol. Sci. Ivyspring International Publisher; 2023 [cited 2025 Apr 11]. pp. 1925–40. Available from: https://doi.org/10.7150/ijbs.76704
51. Zhao B, Li X, Zhou L, Wang Y, Shang P. SIRT1: a potential tumour biomarker and therapeutic target [Internet]. Journal of Drug Targeting. Informa UK Limited; 2019 [cited 2025 Apr 11]. pp. 1046–52. Available from: https://doi.org/10.1080/1061186x.2019.1605519
52. Liu H, Duan C, Yang X, Liu J, Deng Y, Tiselius H-G, Metformin suppresses calcium oxalate crystal-induced kidney injury by promoting Sirt1 and M2 macrophage-mediated anti-inflammatory activation [Internet]. Sig Transduct Target Ther. Springer Science and Business, Media LLC et al. 2023 [cited 2025 Apr 11]. Available from: https://doi.org/10.1038/s41392-022-01232-3
53. Wang X, Song X, Fang K, Chang X. CD38 modulates cytokine secretion by NK cells through the Sirt1/NF-κB pathway, suppressing immune surveillance in colorectal cancer [Internet]. Sci Rep. Springer Science and Business Media LLC; 2024 [cited 2025 Apr 11]. Available from: https://doi.org/10.1038/s41598-024-79008-8
54. Lin S-C, Liao Y-C, Chen P-M, Yang Y-Y, Wang Y-H, Tung S-L, Periostin promotes ovarian cancer metastasis by enhancing M2 macrophages and cancer-associated fibroblasts via integrin-mediated NF-κB and TGF-β2 signaling [Internet]. J Biomed Sci. Springer Science and Business, Media LLC et al. 2022 [cited 2025 Apr 11]. Available from: https://doi.org/10.1186/s12929-022-00888-x
55. Wang J, Bai J, Wang Y, Zhang K, Li Y, Qian H et al. Feruloylated arabinoxylan from wheat bran inhibited M1-macrophage activation and enhanced M2-macrophage polarization [Internet]. International Journal of Biological Macromolecules. Elsevier BV; 2022 [cited 2025 Apr 11]. pp. 993–1001. Available from: https://doi.org/10.1016/j.ijbiomac.2021.11.158

Publisher's note